Xia X, Liang Q, Ming X, Hou J. An efficient and stable hydrodynamic model with novel source term discretisation schemes for overland flow and flood simulations. *Water Resources Research* 2017, 53. DOI: 10.1002/2016WR020055

AGU PUBLICATIONS

Water Resources Research

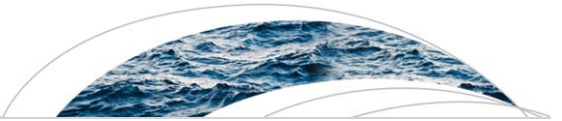

RESEARCH ARTICLE

10.1002/2016WR020055

Key Points:
- A novel surface reconstruction method developed for hydrodynamic overland flow modeling with improved numerical accuracy and stability
- An implicit scheme for discretizing nonlinear friction terms to achieve the correct flow equilibrium at disappearing water depth
- A new local bed modification technique is further introduced to preserve the lake at rest solution

Correspondence to:
Q. Liang,
qiuhua.liang@ncl.ac.uk

Citation:
Xia, X., Q. Liang, X. Ming, and J. Hou (2017), An efficient and stable hydrodynamic model with novel source term discretization schemes for overland flow and flood simulations, *Water Resour. Res.*, *53*, doi:10.1002/2016WR020055.

Received 3 NOV 2016
Accepted 6 APR 2017
Accepted article online 11 APR 2017

An efficient and stable hydrodynamic model with novel source term discretization schemes for overland flow and flood simulations

Xilin Xia[1], Qiuhua Liang[1], Xiaodong Ming[1], and Jingming Hou[1,2]

[1]School of Civil Engineering and Geosciences, Newcastle University, Newcastle Upon Tyne, UK, [2]School of Water Resources and Hydro-Power Engineering, Xi'an University of Technology, Xi'an, China

Abstract Numerical models solving the full 2-D shallow water equations (SWEs) have been increasingly used to simulate overland flows and better understand the transient flow dynamics of flash floods in a catchment. However, there still exist key challenges that have not yet been resolved for the development of fully dynamic overland flow models, related to (1) the difficulty of maintaining numerical stability and accuracy in the limit of disappearing water depth and (2) inaccurate estimation of velocities and discharges on slopes as a result of strong nonlinearity of friction terms. This paper aims to tackle these key research challenges and present a new numerical scheme for accurately and efficiently modeling large-scale transient overland flows over complex terrains. The proposed scheme features a novel surface reconstruction method (SRM) to correctly compute slope source terms and maintain numerical stability at small water depth, and a new implicit discretization method to handle the highly nonlinear friction terms. The resulting shallow water overland flow model is first validated against analytical and experimental test cases and then applied to simulate a hypothetic rainfall event in the 42 km^2 Haltwhistle Burn, UK.

1. Introduction

Numerical simulation of overland flows is essential for better understanding the transient processes of flash floods in a catchment. Traditionally, hydrological models or simplified hydrodynamic models [*Lighthill and Whitham*, 1955; *Govindaraju*, 1988; *Bates et al*., 2010] are usually used for overland flow simulations at a catchment scale. However, most of these simplified models are not capable of depicting the rapid catchment responses and the highly transient surface flow processes to accurately predict water depths and velocities the flood waves [e.g., *Cea et al*., 2010; *Costabile et al*., 2012]. Moreover, their reduced representation of physical complexity may lead to increased sensitivity to parameterization. In recent years, hydrodynamic simulation of overland flows based on the solution to the fully 2-D shallow water equations (SWEs) has become increasingly popular [e.g., *Fiedler and Ramirez*, 2000; *Sanders et al*., 2008; *Simons et al*., 2014; *Yu and Duan*, 2014; *Cea and Blade*, 2015; *Rousseau et al*., 2015; *Caviedes-Voullième et al*., 2012; *Liang et al*., 2015]. Particularly, the Godunov-type SWE models have presented great potential for modeling transient overland flows and flash floods due to their automatic shock-capturing capability [e.g., *Cea and Vazquez-Cendon*, 2010; *Yu and Duan*, 2014].

Unlike fluvial floods or dam breaks in which the inundation areas are usually confined within the floodplain of a river channel or tsunamis in which the flood depth is significant, rainfall-induced overland flows involve very shallow downhill flows on hill slopes. As a result, rainfall-induced overland flows commonly have two distinctive features: (1) most of the domain is wet regardless of the local topography, which implies that flow can develop over highly irregular topography with steep/abrupt slopes, e.g., riverbank or building roof; and (2) water depth may be very small (at the order of centimeters) over a large part of the problem domain. These flow features essentially impose new challenges for developing efficient and stable numerical schemes for solving the SWEs in the context of large-scale overland flow simulations.

The first challenge is related to the discretization of slope source terms for simulating very shallow flows over steep and irregular slopes. Numerous numerical schemes [e.g., *Greenberg and Leroux*, 1996; *LeVeque*, 1998; *Garcia-Navarro and Vazquez-Cendon*, 2000; *Zhou et al*., 2001; *Rogers et al*., 2003; *Audusse et al*., 2004; *George*, 2008; *LeFloch and Thanh*, 2011; *Murillo and García-Navarro*, 2010; *Kesserwani and Liang*, 2011;

Chertock et al., 2015] have been developed to enhance the accuracy and stability for solving the SWEs with bed slope source terms. An example is the scheme proposed by *Audusse et al*. [2004], in which the Riemann variables are modified before solving the corresponding Riemann problem to preserve the lake at rest solution and positivity of water depth. Another feature of this scheme is that the computed bed slope is constrained by an upper bound determined by water depth. This feature can be useful when dealing with discontinuous topography. At places like river banks and building walls, large velocities may be calculated due to the large slope gradient at the place of discontinuity. These large velocities, which will inevitably slow down a simulation due to the use of small time steps, are indeed unphysical because the SWEs are not valid for excessively steep slopes. In the numerical scheme proposed by *Audusse et al*. [2004], the technique that constrains the slope gradients can effectively avoid large velocities and thus enable stable and efficient simulations. The techniques of premodifying Riemann variables and constraining slope gradients are widely adopted by other researchers to develop SWE-based models [e.g., *Liang and Borthwick*, 2009; *Duran et al*., 2013; *Duran*, 2015; *Bouchut and de Luna*, 2010]. These models appear to be efficient and stable for simulations involving wetting and drying and have been widely used in practical applications [e.g., *Hou et al*., 2013a; *Wang et al*., 2011; *Marche et al*., 2007; *Mangeney et al*., 2007; *Liang et al*., 2015]. A number of other effective numerical schemes [e.g., *George*, 2008; *Murillo and García-Navarro*, 2010] have also been reported in the literature, which apply similar slope gradient constrained technique at the wet-dry interfaces but directly solve the Riemann problems incorporating source terms. As it has been already stated, discontinuous topographic features may exist in overland flow simulations and affect numerical stability even when the domain is fully wet. Therefore, constraining slope gradients over the whole domain seems to be inevitable to maintain the overall stability of an overland flow model. However, as reported in *Delestre et al*. [2012], constraining slope gradients using the aforementioned approaches may lead to incorrect calculation of bed slopes and subsequently velocities of shallow flows running downhill. This unfortunately is a common situation in overland flow simulations.

Another challenge for developing a robust SWE-based overland flow model is related to the discretization of friction source terms. The friction source terms are usually expressed as a nonlinear function of the flow velocity and depth, e.g., the Manning equation. Their nonlinear nature tends to relax the flow velocity toward an equilibrium state. In section 3, we will show that the local equilibrium between friction and bed slope can be reached much faster than the time step determined by the CFL condition in practical overland flow simulations involving small water depth. A numerical scheme must use very small time steps to maintain numerical stability under such a situation, leading to prohibitive computational cost. Several implicit schemes have been developed to handle the "stiff" friction source terms and maintain numerical stability [e.g., *Fiedler and Ramirez*, 2000; *Liang and Marche*, 2009; *Costabile et al*., 2013]. However, numerical instability is not the only concern, relaxation toward the correct equilibrium state is also an important aspect that must be reinforced for correct calculation of overland flows because the dynamics of overland flows is typically controlled by the local equilibrium between friction and bed slope. Therefore, it is important to ensure that a numerical scheme for solving the SWEs can effectively relax the flow toward the equilibrium state in a single time step if the relaxation time scale is much smaller than the hydrodynamic time scale indicated by the CFL condition [*Jin*, 2012; *Teyssier*, 2014].

The choice of Riemann solvers also requires careful consideration. A Riemann solver coupled with the slope source terms, such as the augmented Riemann solver [*George*, 2008], may overestimate the discharge for subcritical flows with nonzero friction, as shown later in section 3. Several attempts have been reported in the mathematics literature to provide a preliminary theoretical background for solving the hyperbolic systems with stiff relaxation [e.g., *Liu*, 1987; *Chen et al*., 1994; *Jin*, 2012]. But further research effort is still needed to resolve the issue of implementing effective schemes for discretizing friction source terms for practical overland flow simulations.

In summary, to address the challenges as mentioned above, a model solving the SWEs for overland flow simulations should

1. approximate correctly slope gradients even in the limit of vanishing water depth;
2. avoid excessively large velocities in places where bed elevation changes abruptly (e.g., building walls and river banks);
3. be able to relax the flow velocity to the equilibrium state in a single time step when the relaxation time scale is much smaller than the hydrodynamic time scale; and

4. predict correctly flow discharge on slopes in the presence of nonzero friction.

Satisfying these requirements are essential for a SWE model to provide acceptable numerical accuracy, stability, and efficiency for overland flow simulations, especially for the cases involving water of small depth flowing downhill. Meanwhile, other essential numerical properties, including the preservation of lake at rest solution and nonnegativity of water depth, should not be compromised. This paper therefore aims to discuss the challenges encountered by overland flow simulations and present a new SWE-based overland flow model that satisfies the aforementioned requirements simultaneously. A novel surface reconstruction method (SRM) is developed to correctly calculate the bed slope gradient in the limit of disappearing water depth and maintain stable simulations in the presence of abrupt bed changes. The friction source terms are discretized using an implicit method that is able to relax the velocity to the correct equilibrium state in a single time step. The rest of the paper is organized as follows: section 2 introduces the governing equations, i.e., the fully 2-D SWEs; section 3 provides a brief review of the relevant numerical schemes and revisits the aforementioned challenges for overland flow simulations; section 4 presents the details of the proposed numerical scheme; the resulting overland flow model is then validated against several test cases in section 5; and finally brief conclusions are drawn in section 6.

2. Governing Equations

The matrix form of the 2-D SWEs with source terms may be written as

$$\frac{\partial \mathbf{q}}{\partial t}+\frac{\partial \mathbf{f}}{\partial x}+\frac{\partial \mathbf{g}}{\partial y}=\mathbf{R}+\mathbf{S}_b+\mathbf{S}_f \tag{1}$$

where $\mathbf{q}$ contains the flow variables; $\mathbf{f}$ and $\mathbf{g}$ are the flux vector terms in the x and y directions; and $\mathbf{R}$, $\mathbf{S}_b$, and $\mathbf{S}_f$ are the source terms representing respectively the rainfall rate, bed slope, and frictional effect. The vector terms are given by

$$\begin{gathered}\mathbf{q}=\begin{bmatrix} h \\ uh \\ vh \end{bmatrix} \mathbf{f}=\begin{bmatrix} uh \\ u^2h+\frac{1}{2}gh^2 \\ uvh \end{bmatrix} \mathbf{g}=\begin{bmatrix} vh \\ uvh \\ v^2h+\frac{1}{2}gh^2 \end{bmatrix} \\ \mathbf{R}=\begin{bmatrix} R \\ 0 \\ 0 \end{bmatrix} \mathbf{S}_b=\begin{bmatrix} 0 \\ -gh\frac{\partial b}{\partial x} \\ -gh\frac{\partial b}{\partial y} \end{bmatrix} \mathbf{S}_f=\begin{bmatrix} 0 \\ -\frac{\tau_{bx}}{\rho} \\ -\frac{\tau_{by}}{\rho} \end{bmatrix}\end{gathered} \tag{2}$$

where g is the gravitational acceleration, h is the water depth, b is the bed elevation, u and v are the depth-averaged velocities along the x and y directions, R is the rainfall rate, ρ is the water density, and τ_{bx} and τ_{by} are the frictional stresses estimated using the Manning formula:

$$\tau_{bx}=\rho C_f u\sqrt{u^2+v^2}\ \ \tau_{by}=\rho C_f v\sqrt{u^2+v^2} \tag{3}$$

in which C_f is the roughness coefficient evaluated using

$$C_f=gn^2/h^{1/3} \tag{4}$$

where n is the Manning coefficient. If the water depth is very small ($\sim 10^{-3}$ m), surface tension and capillary waves may become important. But they are currently not explicitly considered in this work. Instead, their effects are all packed into the Manning's friction terms.

3. A Brief Review of the Existing Numerical Schemes

In this section, we give a brief review of certain existing numerical schemes solving the SWEs for overland flow simulations. However, there is no intention to provide an exhausted review herein and we will limit our

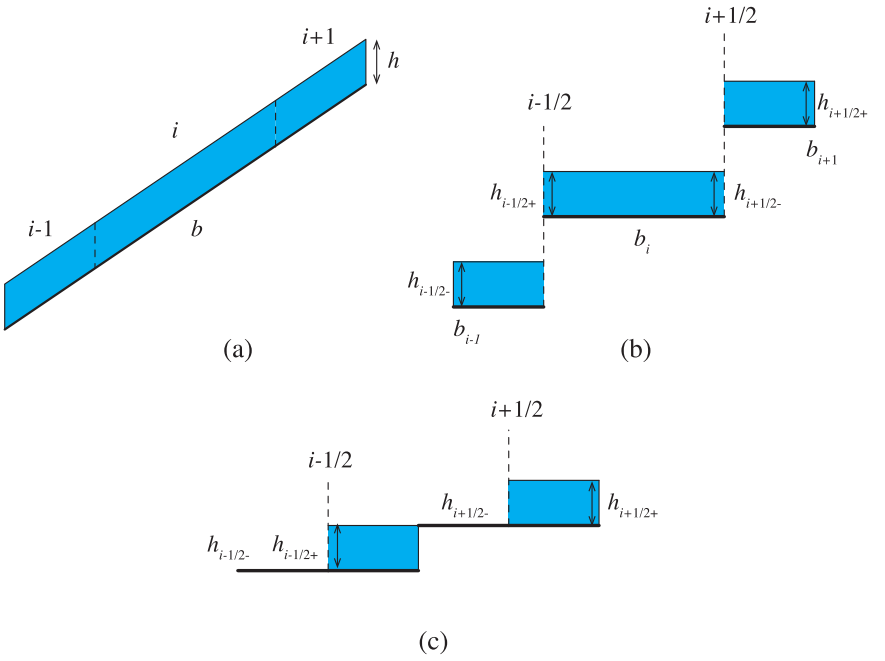

Figure 1. The bed reconstruction method of the typical well-balanced schemes where *h* and *b* respectively denote the water depth and bed elevation: (a) idealized overland flow over a constant slope; (b) the same case at the discretized level; and (c) face values of the water depth and bed elevation after reconstruction.

scope to those prevailing and representative schemes and further explain the challenges as mentioned in section 1.

3.1. Discretization of Bed Slope Terms

For solving the SWEs for overland flow modeling, the first effective numerical scheme to be mentioned herein is the hydrostatic reconstruction method introduced in *Audusse et al*. [2004]. Along the *x* direction, let *i* and $i+1$ denote the two adjacent cells under consideration. The first step of hydrostatic reconstruction is to define a single bed elevation at the cell interface as

$$b_{i+1/2}=\max\left(b_i, b_{i+1}\right) \tag{5}$$

based on which the Riemann states of water depth across the cell interface are defined as

$$h_{i+1/2-}=\max\left(h_i+b_i-b_{i+1/2}, 0\right) \ , \ h_{i+1/2+}=\max\left(h_{i+1}+b_{i+1}-b_{i+1/2}, 0\right) \tag{6}$$

The corresponding bed slope source term is subsequently derived and discretized to become

$$S_{bx}=\left(\frac{1}{2}gh_{i+1/2-}^2-\frac{1}{2}gh_{i-1/2+}^2\right)/\Delta x \tag{7}$$

where Δx is the cell size. This scheme preserves exactly the lake at rest solution and the positivity of water depth if an appropriate Riemann solver is adopted. Equation (7) may be reformulated as follows:

$$S_{bx}=-\frac{1}{2}g\left(h_{i+1/2-}+h_{i-1/2+}\right)\frac{h_{i-1/2+}-h_{i+1/2-}}{\Delta x} \tag{8}$$

where $\frac{h_{i-1/2+}-h_{i+1/2-}}{\Delta x}$ may be viewed as the discretization of the term related to bed slope, i.e., $\frac{\partial b}{\partial x}$. Apparently, no matter how steep the actual bed slope is, the computed value for $\frac{\partial b}{\partial x}$ is $\frac{h_{i-1/2+}-h_{i+1/2-}}{\Delta x}$, which essentially imposes a constrained condition on the bed slope gradient. Although this effectively avoids the large velocities that would otherwise occur when the bed slope is excessively steep, it unfortunately also introduces certain unwanted side effects for overland flow simulation which will be explained as follows.

Consider a simple case of uniform flow (with a fixed depth) over a constant slope, as illustrated in Figure 1a. The water depth is smaller than the difference of bed elevation between the two neighboring cells, i.e.,

$h < b_{i+1} - b_i$. In such a case, the computed bed slope from (6) is clearly milder than the actual slope, as shown in Figures 1b and 1c. Following this constrained slope reconstruction, the water depth defined from (6) is always zero at the left-hand side of a cell interface for this case, as illustrated in Figure 1c. The local Riemann problem essentially defines a dry-bed dam break and the localized flow condition has been artificially reconstructed to become a waterfall rather than a uniform flow, which is physically incorrect and may lead to misleading prediction. The immediate effects are (1) water can only move in one direction, and (2) the forward-moving signal speed becomes associated with a dry-bed dam break, which is much larger than the flow velocity and will lead to overestimation of the discharge (see section A1). Numerically, it may somehow compensate the underestimation of discharge due to the constrained slope gradient, but the exact amount is difficult to quantify. In the rest of this text, this numerical phenomenon is referred to as "waterfall effect." Research efforts [e.g., *Morales De Luna et al*., 2013; *Hou et al*., 2014] have been devoted to resolve this issue of incorrect discretization of bed slope terms in the original hydrostatic reconstruction method. But all of the reported modified hydrostatic reconstruction methods still suffer from modifying water depth to zero at one side of a cell interface for the case as illustrated in Figure 1, and the problem of "waterfall effect" persists.

The idea of constraining slope gradients is also used in other numerical schemes [e.g., *Liang and Borthwick*, 2009; *Bouchut and de Luna*, 2010; *Song et al*., 2011a]. Although the specific formulations may be different, these approaches tend to encounter the same problem as previously mentioned [*Delestre et al*., 2012]. The issue related to the incorrect discretization of bed slope terms is particularly problematic for the first-order schemes. However, the higher order schemes may not be immunized because it is a common practice to reduce a scheme to be first-order accurate when the predicted water depth becomes smaller than certain thresholds, in order to stabilize a simulation [e.g., *Hou et al*., 2013b; *Song et al*., 2011b; *Murillo et al*., 2007; *Liang*, 2010]. There are some numerical schemes [e.g., *George*, 2008; *Murillo and García-Navarro*, 2010] that do not impose a constraint on the slope source terms except at the wet-dry front. While these schemes do not underestimate the slope source terms as the hydrostatic reconstruction does, they also lose the advantage provided by the constrained slope gradients, in terms of stabilizing a simulation over irregular topography with abrupt bed changes.

3.2. Discretization of Friction Terms

We have mentioned in section 1 that it is essential for a numerical scheme solving the SWEs to relax the flow toward an equilibrium state, in order to correctly describe an overland flow when the water depth becomes small and the friction effect becomes predominant. Considering a 1-D problem and assuming a positive velocity, the physical equilibrium velocity as a result of balanced bed slope and friction terms can be obtained as

$$u_\infty = \sqrt{\frac{S_{bx}}{gn^2 h^{-1/3}}} \tag{9}$$

The time scale controlling the relaxation toward such an equilibrium is given by

$$t_f = \frac{1}{h^{-1}\partial S_{fx}/\partial u} = \frac{1}{2gn^2 h^{-4/3} u} \tag{10}$$

The hydrodynamic time scale, i.e., the time scale that the flow property in a cell can be updated (due to convection), may be characterized by the time step determined by the CFL condition

$$t_{HD} = \frac{\Delta x}{u + \sqrt{gh}} \tag{11}$$

The ratio between these two difference time scales is

$$\frac{t_f}{t_{HD}} = \frac{u + \sqrt{gh}}{2\Delta x g n^2 h^{-4/3} u} \tag{12}$$

Considering the typical values of the flow variables or parameters that may be encountered in practical overland flow simulations, e.g., $\Delta x \sim 10$ m, $h \sim 0.01$ m, $n \sim 0.03$ s m$^{-1/3}$, and $u \sim \sqrt{gh}$, the ratio $\frac{t_f}{t_{HD}}$ is about 0.024, which implies that from a physical point of view the local equilibrium between friction and bed slope can be reached much faster than the typical time step determined by the CFL condition. In order

to correctly predict overland flows when the water depth becomes small and the friction effect becomes predominant, a numerical scheme must be able to relax the flow velocity to the correct equilibrium state numerically in a single time step.

A conventional way to discretize the friction source terms is achieved using implicit schemes. In practice, implicit discretization is often reformulated to derive an effective explicit scheme. Considering a 1-D problem, many schemes [e.g., *Song et al*., 2011a; *Busaman et al*., 2015; *Cea and Blade*, 2015; *Cea and Vazquez-Cendon*, 2010; *Burguete et al*., 2008; *Liang et al*., 2006; *Costabile et al*., 2013; *Singh et al*., 2015; *Rousseau et al*., 2015] adopt the following discretized equations

$$\hat{q}_x^{n+1} = q_x^n - \frac{\Delta t}{\Delta x}\left(F_{i+1/2}^n - F_{i-1/2}^n\right) + \Delta t S_{bx}^n \tag{13}$$

$$q_x^{n+1} = \frac{\hat{q}_x^{n+1}}{1 + \Delta t g n^2 \left(h^n\right)^{-4/3} |u^n|} \tag{14}$$

where $q_x = hu$ is the unit discharge in the x direction, F is the momentum flux term, S_{bx} is the bed slope term, and Δt is the time step. For the implicit scheme as described in (13) and (14), the local acceleration (flux) term becomes small and negligible when the friction term is predominant. Considering that the relaxation time scale is much smaller than the hydrodynamic time scale, (14) can be rescaled by taking $\Delta t \to \infty$. The velocity resulting from the scheme is

$$\hat{u}_\infty = \frac{S_{bx}}{g n^2 h^{n+1} \left(h^n\right)^{-4/3} |u^n|} \tag{15}$$

Apparently $\hat{u}_\infty$ is not equal to the physical equilibrium u_∞ given in (9), and therefore (13) and (14) cannot relax the velocity to the correct equilibrium state in a single time step.

Fractional splitting method has also been used for computing friction source terms. For example, *Liang and Marche* [2009] proposed the following scheme

$$q_x^{n+1} = q_x^* + \frac{\Delta t S_{fx}^*}{1 + 2\Delta t g n^2 \left(h^*\right)^{-4/3} |u^*|} \tag{16}$$

where h^*, q_x^*, and u^* are updated from the previous time step by solving the frictionless SWEs, S_{fx}^* is the friction term calculated from h^*, q_x^*, and u^*. The velocity for $\Delta t \to \infty$ is

$$\hat{u}_\infty = \frac{1}{2} u^* \tag{17}$$

which again does not give the correct equilibrium state.

A few numerical schemes also impose an upper bound on the friction terms [e.g., *Burguete et al*., 2008; *Liang and Marche*, 2009] so that the friction does not reverse the flow direction, which leads to $\hat{u}_\infty = 0$ and again is different from the correct equilibrium state. The scheme reported by *Yu and Duan* [2014] manually set the velocity to the equilibrium state as long as the kinematic wave number is larger than a threshold, but the criteria to determine the threshold may be case dependent, restricting its robustness for applications.

The existence of the predominant friction terms may also affect the validity of existing Riemann solvers for simulating rainfall-induced overland flows running downhill. In an extreme case, the discharge on a slope can be significantly overestimated as already briefly mentioned in section 1. Herein the augmented Riemann solver introduced by *George* [2008] is taken as an example for further analysis. This Riemann solver is implemented in the framework of the wave propagation algorithm proposed by *LeVeque* [1997] and has become part of the open-source GeoClaw software [*Berger et al*., 2011]. The time-marching formula in the wave propagation algorithm is given as

$$\mathbf{q}_i^{n+1} = \mathbf{q}_i^n - \frac{\Delta t}{\Delta x}\left(\mathcal{A}^+ \Delta Q_{i-1/2} + \mathcal{A}^- \Delta Q_{i+1/2}\right) \tag{18}$$

where $\mathcal{A}^\pm \Delta Q$ is defined as the fluctuations at the cell interface that are determined by solving a general Riemann problem including initial bed elevation discontinuity. The mass flux, i.e., unit discharge across cell interface $i+1/2$ can be expressed by the fluctuations (see section A2 for detailed derivation) as

$$F^h_{i+1/2} = \mathcal{A}^- \Delta H_{i+1/2} + hu_i \tag{19}$$

where $\mathcal{A}^{\pm}\Delta H$ is the mass fluctuations. Considering the simple case of steady flow running downhill with a uniform discharge and a uniform depth in which the bed slope is balanced by the friction slope, the analysis in section A2 shows that $\mathcal{A}^- \Delta H_{i+1/2} > 0$ if the flow is subcritical and $b_i > b_{i+1}$. In such a case, it can be obviously seen from (19) that $F^h_{i+1/2} > hu_i$, i.e., the mass flux computed at the cell interface by the Riemann solver is larger than the cell-centered discharge. Although the increase of velocity due to the slope source term can be balanced by the friction effect during the time integration, the overestimated mass flux across cell interface cannot be eliminated by the friction effect, which leads to more water flowing across the cell interface than the reality. For Riemann solvers coupled together with the bed slope source terms, the bed discontinuity at the cell interface needs to generate a mass flux to balance the mass flux cause by the discontinuous water depth to maintain the lake at rest solution. But for steady flow featured by the balance between the bed slope and the friction slope, such a mass flux generated by the bed discontinuity becomes a source of error. It is very likely that certain other schemes such as the upwind treatment of bed slope [*Bermúdez et al*., 1998] and the lateralized HLL Riemann solver [*Fraccarollo et al*., 2003] encounter the same problem of overestimating the mass flux. In practical applications, this will speed up the overland flows from hillslopes to river channels and consequently predict earlier arrival of flood peaks. One way to resolve this problem is to incorporate the friction source terms into the Riemann solver, but this is outside the scope of this paper.

Other Riemann solvers that have been widely applied to solve the homogeneous SWEs such as the HLL or HLLC solver, do not seem to suffer from this problem. Because the HLL or HLLC Riemann solver is not coupled with the slope source terms, the calculated mass flux $F^h_{i+1/2}$ is equivalent to the cell-centered discharge hu_i. The mass flux remains to be the original discharge as long as the increase of velocity induced by the bed slope is correctly balanced by the friction effect during time integration. But a numerical scheme implemented with the HLL or HLLC Riemann solver may suffer from the aforementioned inaccurate calculation of slope source terms or waterfall effect, which must be overcame by incorporating with a proper slope source term discretization scheme.

4. Numerical Scheme

In this section, a novel first-order Godunov-type finite volume scheme is presented to address the aforementioned challenges in the context of overland flow and surface flood simulations.

4.1. Finite Volume Discretization

A finite volume scheme solves the integrated form of governing equations and the resulting semidiscretized equation is given by

$$\frac{\partial \mathbf{q}_i}{\partial t} + \frac{1}{\Omega_i}\sum_{k=1}^{N} \mathbf{F}_k(\mathbf{q}) l_k = \mathbf{R}_i + \mathbf{S}_{bi} + \mathbf{S}_{fi} \tag{20}$$

where "i" is the cell index, "k" is the index of the cell edges ($N = 4$ for Cartesian grids as adopted in this work), l_k is the length of cell edge "k," and Ω_i is the cell area, $\mathbf{F}_k(\mathbf{q}) = \mathbf{f}_k(\mathbf{q}) n_x + \mathbf{g}_k(\mathbf{q}) n_y$ contains the fluxes normal to the cell boundary with $\mathbf{n} = (n_x, n_y)$ defining the outward normal direction at the cell boundary. Herein, the fluxes $\mathbf{F}$ and slope source terms $\mathbf{S}_b$ are computed explicitly, but the friction source terms $\mathbf{S}_f$ are treated implicitly. The final time-marching scheme is given as

$$\mathbf{q}^{n+1} = \mathbf{q}^n - \frac{\Delta t}{\Omega_i}\sum_{k=1}^{N} \mathbf{F}_k(\mathbf{q}^{\mathbf{n}}) l_k + \Delta t(\mathbf{R}^n_i + \mathbf{S}^n_{bi} + \mathbf{S}^{n+1}_{fi}) \tag{21}$$

in which n denotes the time level and Δt is the time step. The asymptotic behavior of the discretized equation may be analyzed as follows: as $h \to 0$, it is straightforward to infer from nondimensionalization analysis that the convective flux term $\mathbf{F}(\mathbf{q})$ is much smaller than other terms and therefore negligible; the corresponding relaxation time is typically very small compared with the time step determined by the CFL condition and therefore $\Delta t \to \infty$, which is equivalent to rescaling the equations; subsequently, (21) reduces to the following equilibrium equation:

$$\mathbf{S}_{bi}^{n}+\mathbf{S}_{fi}^{n+1}=0 \tag{22}$$

where the rainfall source term has been omitted because only the momentum equations are relevant to the analysis. The flow velocities at the new time step can then be recovered from (22) as

$$\mathbf{u}^{n+1}=\sqrt{\frac{||\mathbf{S}_{bi}^{n}||}{C_f}}\cdot\frac{\mathbf{S}_{bi}^{n}}{||\mathbf{S}_{bi}^{n}||} \tag{23}$$

This is basically the 2-D form of the equilibrium state as defined in (9). Equation (23) does not imply that the flow is steady at the beginning. Instead, it is the result of rescaling the equation by considering that the relaxation time scale is much smaller than the hydrodynamic time scale. Therefore, (21) is able to relax the velocity to the equilibrium state in a single time step when $h \rightarrow 0$ as long as the implicit part of (21) is solved exactly. Note that the use of implicit schemes as (13)–(14) and (16) does not ensure the recovery of the correct equilibrium state because the implicit schemes have been reformulated into explicit forms and the implicit part is no longer solved exactly.

4.2. Interface Fluxes and Slope Source Term Discretization

As discussed in the previous section, the augmented Riemann solvers [e.g., *George*, 2008] may lead to overestimated discharge on slopes. The classic Riemann solvers that solve the homogeneous SWEs appear to be a more suitable choice and an HLLC approximate Riemann solver is adopted to calculate the interface fluxes in (21) [see *Liang and Borthwick*, 2009; *Toro*, 2001 for detailed implementation]. The HLLC Riemann solver does not automatically preserve the lake at rest solution and it is necessary to implement the hydrostatic reconstruction scheme [*Audusse et al.*, 2004] or other effective approaches to modify the Riemann states before solving the local Riemann problems. In this section, a novel surface reconstruction method (SRM) is proposed to integrate with hydrostatic reconstruction to obtain the Riemann states to define the local Riemann problems across cell interfaces and overcome the limitations of the existing hydrostatic reconstruction implementations. Specifically, SRM can effectively (1) avoid the "waterfall effect" when evaluating the fluxes; (2) preserve the original bed slope when necessary for correct prediction of flow velocities; and (3) constrain the bed slope only for the cases where the topography is "genuinely" discontinuous to maintain stability.

To implement the proposed SRM, the water surface elevation (defined in an arbitrary cell "i" as $\eta_i=h_i+b_i$) at cell interfaces is first reconstructed to support the derivation of Riemann states. Considering two adjacent cells "i" and "$i+1$," the SRM reconstructed water surface elevations at left-hand and right-hand sides of their common interface are given by

$$\begin{cases}\eta_L=\eta_i+\max\left[0,\min\left(b_{i+1}-b_i-\delta b,\eta_{i+1}-\eta_i\right)\right]\\ \eta_R=\eta_{i+1}+\max\left[0,\min\left(b_i-b_{i+1}+\delta b,\eta_i-\eta_{i+1}\right)\right]\end{cases} \tag{24}$$

with

$$\delta b=b_{i+1/2+}-b_{i+1/2-} \tag{25}$$

where $b_{i+1/2+}$ and $b_{i+1/2-}$ are respectively the bed elevation at the right-hand and left-hand sides of the cell interface, obtained through slope limited interpolation of the related cell center values

$$b_{i+1/2-}=b_i+\mathbf{r}_i\Psi(r_i)\nabla b_i\,,\ b_{i+1/2+}=b_{i+1}+\mathbf{r}_{i+1}\Psi(r_{i+1})\nabla b_{i+1} \tag{26}$$

where $\mathbf{r}$ is the distance vector from the cell center to central point of the cell interface, $\Psi(r)\nabla b_i$ is the bed gradient restricted by a minmod slope limiter that is defined on a rectangular Cartesian grid for cell "i" as

$$\Psi(r_i)=\max\left[0,\min\left(r_i,1\right)\right]\text{ and }r_i=\frac{f_+-f_i}{f_i-f_-} \tag{27}$$

in which the subscripts + and – denote the upstream and downstream cells, respectively. The interpolated bed elevations are only calculated at the beginning of a simulation to reduce computational cost. The use of a slope limiter herein is crucial for distinguishing the discontinuous and smooth topographies and applying the constraint to the slope gradient at the right place.

From the reconstructed water levels in (24), the corresponding states of bed elevation at the left-hand and right-hand sides of the cell interface can be obtained as

$$\begin{cases} b_L = \eta_L - h_i \\ b_R = \eta_R - h_{i+1} \end{cases} \tag{28}$$

The Riemann states can then be deduced by first defining a single bed elevation at the cell interface, as suggested by *Audusse et al*. [2004]

$$b_f = \max(b_L, b_R) \equiv \max(b_i, b_{i+1}) \tag{29}$$

based on which the Riemann states of water depth are defined as

$$\begin{cases} h_L = \max(0, \eta_L - b_f) \\ h_R = \max(0, \eta_R - b_f) \end{cases} \tag{30}$$

which reinforces the nonnegativity of water depth. The Riemann states of the other flow variables (i.e., unit-width discharges) are subsequently obtained

$$\begin{cases} [hu]_L = h_L u_i, & [hv]_L = h_L v_i \\ [hu]_R = h_R u_{i+1}, & [hv]_R = h_R v_{i+1} \end{cases} \tag{31}$$

where $u_i = [hu]_i / h_i$ and $u_{i+1} = [hu]_{i+1} / h_{i+1}$ (similarly v_i and v_{i+1}) are the velocities defined at the cell center.

It should be noted that (24) has an asymmetric form so that it only modifies the lower water surface elevation between the two. It effectively takes into account all different water surface and bed elevation configurations that are possibly encountered in surface flow simulations. Without losing generality, we assume that $b_i < b_{i+1}$. Because the slope gradient is limited by a minmod limiter, the monotonicity of the bed elevations is preserved and we always have $\delta b \geq 0$.

When $\delta b = 0$, i.e., the slope is constant across the four consecutive cells involved in the slope limited reconstruction in (26), there are three possible configurations to consider. Figure 2a illustrates the first case where $b_{i+1} - b_i > \eta_{i+1} - \eta_i > 0$. From (24), we have $\eta_L = \eta_i + (\eta_{i+1} - \eta_i)$ and so the water surface at the left-hand side will be lifted to the same level as that at the right-hand side. Figure 2b presents the second case where $b_{i+1} - b_i < \eta_{i+1} - \eta_i$. From (24), it gives $\eta_L = \eta_i + (b_{i+1} - b_i)$, indicating that the water surface at the left-hand side will be raised to eliminate the difference between the bed elevations. Finally, the third case involves $\eta_{i+1} - \eta_i \leq 0$, as shown in Figure 2c, where (24) imposes no modification. With the reconstructed water surface elevations, the Riemann states of water depth are obtained through (28)–(30), which are also shown in Figure 2. In all of the three cases, the reconstructed water depths at both sides of the cell interface are nonzero; the direction of fluxes depends on the local flow and topographic conditions. Therefore, SRM effectively avoids the artificial "waterfall effect" created by the specific numerical treatment as found in the prevailing hydrostatic reconstruction implementations [e.g., *Audusse et al*., 2004].

When $\delta b > 0$, there are also different cases to be considered. When $b_{i+1} - b_i - \delta b > \eta_{i+1} - \eta_i > 0$, equation (24) leads to $\eta_L = \eta_i + (\eta_{i+1} - \eta_i)$ and the resulting water surface reconstruction is identical to Figure 2a. Similarly, $\eta_{i+1} - \eta_i \leq 0$ defines the case identical to the one as illustrated in Figure 2c for $\delta b = 0$. When $b_{i+1} - b_i - \delta b < \eta_{i+1} - \eta_i$, as illustrated in Figure 3, equation (24) gives $\eta_L = \eta_i + (b_{i+1} - b_i - \delta b)$, implying that the reconstructed bed elevation b_L on the left-hand side is δb lower than b_R (i.e., b_{i+1}) which is untouched during the reconstruction. This can be also confirmed by identifying the reconstructed bed elevations following (28): $b_L = \eta_L - h_i = b_{i+1} - \delta b$, $b_R = \eta_R - h_{i+1} = b_{i+1}$, and therefore $b_R - b_L = \delta b$, confirming that the variation between the interpolated bed elevations δb is preserved during the reconstruction. With the reconstructed water surface elevation, the Riemann states of the water depth are then defined from (30): $h_L = \max(0, h_i - \delta b)$ and $h_R = h_{i+1}$ as $b_f = b_{i+1}$. Considering $h_L = \max(0, h_i - \delta b)$, it is clear that h_L depends on the magnitude of δb, which essentially quantifies the discontinuity of the bed profile. If the bed curvature is small, δb will be small and it is likely that $\delta b < h_i$, leading to a positive h_L, as shown in Figure 3a. If the bed curvature is large or there is an abrupt change of bed elevation (e.g., a wall or riverbank), δb may likely become larger than h_i, leading to $h_L = 0$, as shown in Figure 3b. In this case, the water can only flow downhill from the higher side, effectively representing the real-world situation.

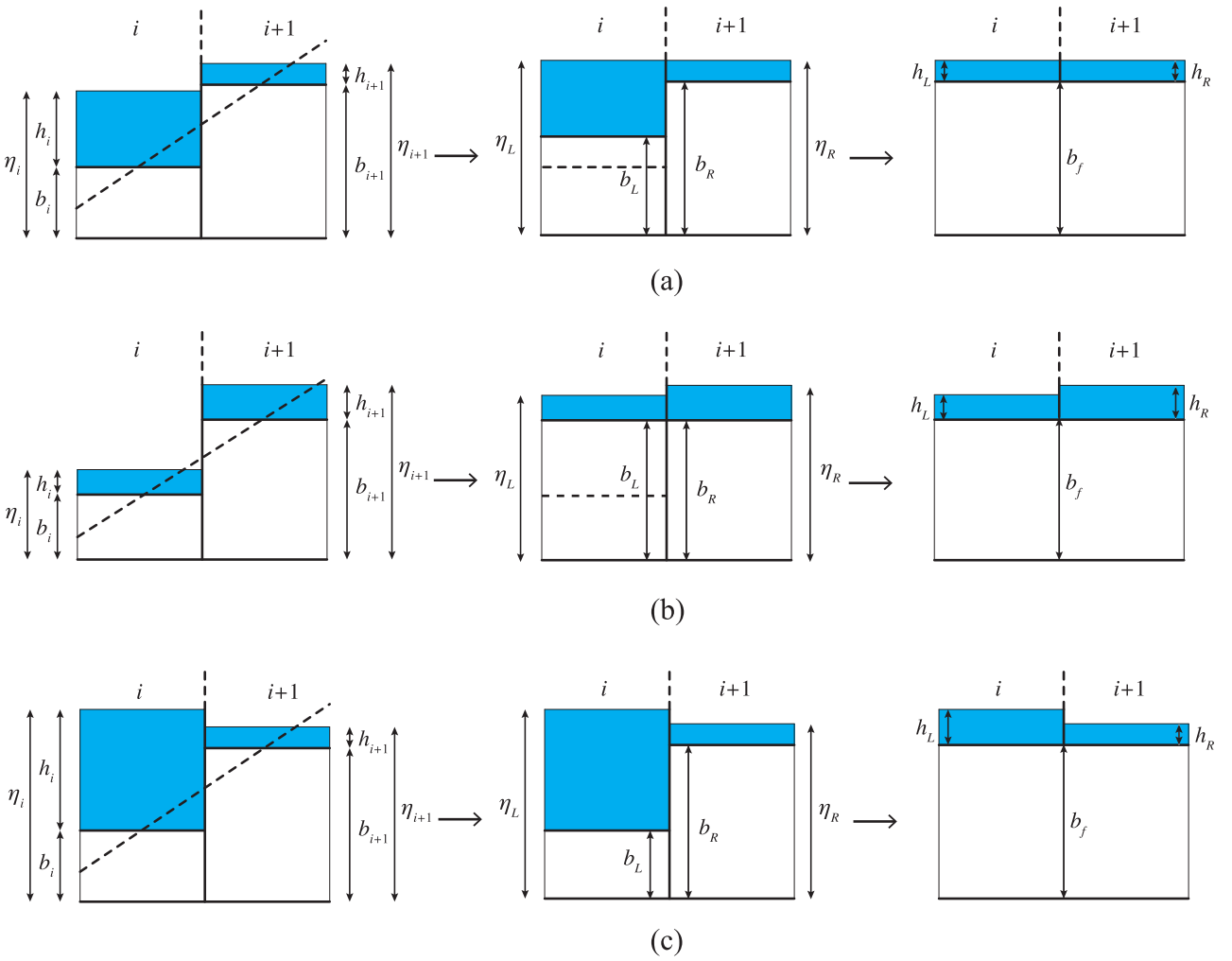

Figure 2. SRM implementation when $\delta b=0$ and (a) $b_{i+1}-b_i > \eta_{i+1}-\eta_i > 0$; (b) $b_{i+1}-b_i < \eta_{i+1}-\eta_i$; and (c) $\eta_{i+1}-\eta_i \leq 0$. Illustration of (left) the original discretization with the dashed line representing the limited slope, (middle) the water surface elevation reconstructed according to (24) with the dashed line representing the original location of the bed, and (right) the Riemann states of water depth defined following (29) and (30).

Another advantage of SRM is that it does not affect the maximum value between b_i and b_{i+1}. Following the definition of the single face value of bed elevation in (28), the genuine bed variation within a cell is effectively preserved during the reconstruction. The bed slope source terms can be simply discretized using the following equation:

$$\mathbf{S}_{bi}=\begin{pmatrix} 0 \\ \frac{1}{\Omega_i}\sum\frac{1}{2}g(h_i+h_{L,k})(b_i-\overline{b}_{f,k})\mathbf{n}_k l_k \end{pmatrix} \tag{32}$$

where $h_{L,k}$ is the left Riemann state of water depth at cell edge "k" and $\overline{b}_{f,k}$ is the modified face value of the bed elevation that will be introduced below.

Considering an arbitrary cell "i," violation of the lake at rest solution and numerical instability may occur during a simulation when the final reconstructed water surface elevation at one of its cell interface is lower than the bed elevation at another cell interface along the same direction. As illustrated in Figure 4, this basically reflects the cases when the flow hits a "wall" or when cell "i" has an excessive slope caused by abrupt change of bed elevation. In order to preserve the lake at rest solutions in the vicinity of wet-dry interfaces and avoid numerical instability caused by abrupt change of bed elevation, the following local bed modification scheme is proposed and applied to all of the computational cells

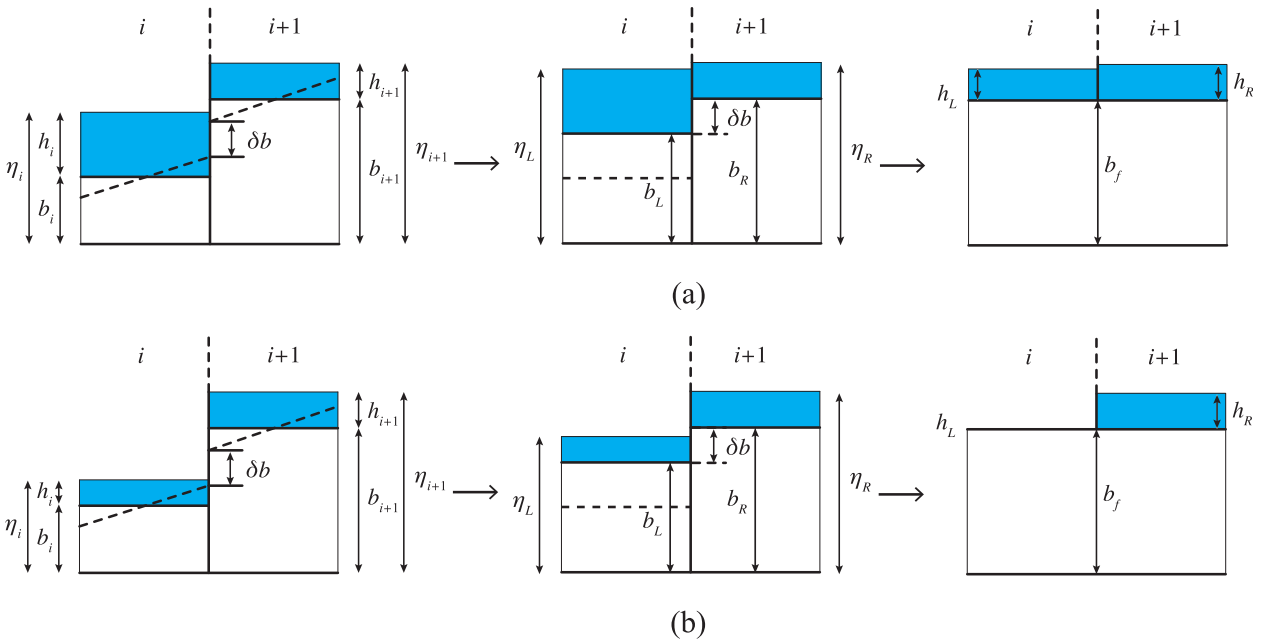

Figure 3. SRM implementation when $\delta b > 0$ and $b_{i+1} - b_i - \delta b < \eta_{i+1} - \eta_i$: (a) $0 < \delta b < h_i$ and (b) $\delta b > h_i$. Illustration of (left) the original discretization with the dashed line representing the limited slope, (middle) the water surface elevation reconstructed according to (24) with the dashed line representing the original location of the bed, and (right) the Riemann states of water depth defined following (29) and (30).

$$\overline{b}_f = b_f - \Delta b \tag{33}$$

$$\begin{cases} \Delta b = \max(0, b_f - \eta_i) & \text{if } h_{i+1} < \varepsilon_h \\ \Delta b = \max(0, \min(\delta b, b_f - \eta_i)) & \text{if } h_{i+1} >= \varepsilon_h \end{cases} \tag{34}$$

where ε_h is an infinitesimal value to define dry cells, which is taken as 10^{-10} m in this work. It should be particularly noted that the original water surface elevation η_i at the cell center rather than the reconstructed

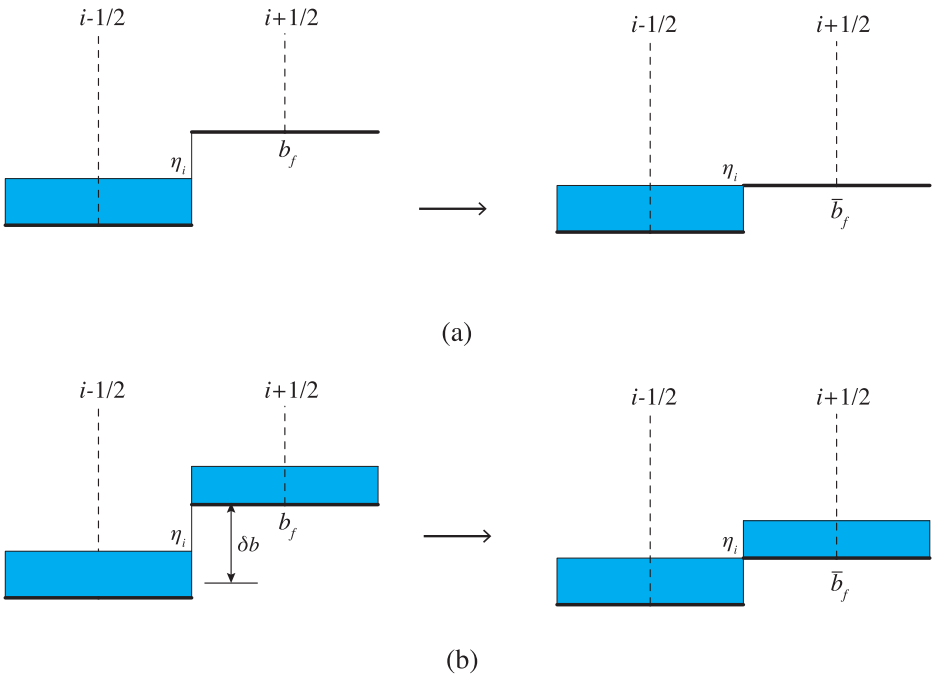

Figure 4. Local modification of interface bed elevation after water surface reconstruction: (a) wet-dry cells and (b) wet-wet cells.

value η_L is used in (34) to calculate Δb. Without losing generality, it is assumed that the reconstructed water surface elevation at the left-hand side cell interface of cell "*i*," i.e., "$i-1/2$," is lower than the bed elevation at the right-hand side cell interface "$i+1/2$." Figure 4a represents the case when the flow hits a "wall," i.e., when cell "*i*" is wet but cell "$i+1$" is dry with a ground level higher than the water surface. With $\Delta b=b_f-\eta_i$, the local bed modification (33) and (34) essentially lowers the bed at cell interface "$i+1/2$" until it becomes horizontal to the reconstructed water surface at "$i-1/2$." This effectively preserves the lake at rest solutions. When both cell "*i*" and cell "$i+1$" are wet, (34) gives $\Delta b=\max(0,\min(\delta b, b_f-\eta_i))$. In a normal condition when the domain topography is smooth or has a constant slope, δb will be small/zero, so does Δb. The proposed local bed modification scheme does not take effects and the computation is undertaken with the bed slope inside cell "*i*" correctly represented. Figure 4b illustrates a case when bed level at cell "$i+1$" changes abruptly and is much higher than the water surface at cell "*i*" (i.e., $\delta b > b_f-\eta_i$), as a result of excessive bed curvature or discontinuous topography. This may lead to numerical instability during a simulation and should be avoided. From (34), we have $\Delta b=b_f-\eta_i$ and then from (34) $\overline{b}_f=b_f-\Delta b=\eta_i$. This effectively removes the excessive slope in cell "*i*" and hence ensures a stable simulation; otherwise, time steps may become prohibitively small due to the large velocities calculated from large slope source terms.

The current numerical method, featured with the aforementioned SRM and local bed modification schemes, strictly preserves the lake at rest solution even when the numerical solution involves wetting and drying over irregular bed topography. This may be proved as follows: for a lake at rest problem with a stationary water surface $\overline{\eta}$, we have $\overline{b}_{f,k}=\overline{\eta}-h_{L,k}$; the momentum components of $\mathbf{S}_{bi}$ in (32) can be rewritten as $\frac{1}{\Omega_i}\sum\left[\frac{1}{2}g(h_i b_i-h_i\overline{\eta}+h_{k,L}^2)\right]\mathbf{n}_k l_k$; the first two terms vanish following simple algebra manipulation and the expression becomes $\frac{1}{\Omega_i}\sum\frac{1}{2}gh_{k,L}^2\mathbf{n}_k l_k$; this effectively balances the momentum fluxes to preserve the lake at rest solution.

4.3. Friction Source Term Discretization

The implicit part of (21) is solved directly rather than reformulated into an explicit form as in (16) to ensure the flow velocities relaxed to the correct equilibrium state in a single time step when the friction becomes predominantly large. Since the continuity equation does not involve a nonzero friction term, the implicit scheme only applies to the momentum equations. The implicit terms in the *x* and *y* direction momentum equations are interdependent, and an iteration method must be used. Denoting the unit-width discharge $\mathbf{Q}_i^{n+1}=([uh]_i^{n+1},[vh]_i^{n+1})^T$, the momentum components of (21) may be rewritten as

$$\mathbf{Q}_i^{n+1}=\mathbf{Q}_i^n+\Delta t(\mathbf{A}_i^n+\mathbf{S}_i^{n+1}) \tag{35}$$

where $\mathbf{A}_i^n=\frac{1}{\Omega_i}\sum_{k=1}^{N}\mathbf{F}_k(\mathbf{q}^{\mathbf{n}})l_k+\mathbf{S}_{bi}^n$ represents the momentum components of the convective fluxes and slope source terms and $\mathbf{S}_i^{n+1}$ contains the friction source terms for the momentum equations given by

$$\mathbf{S}_i^{n+1}=-gn^2(h_i^n)^{-7/3}\mathbf{Q}_i^{n+1}|\mathbf{Q}_i^{n+1}| \tag{36}$$

When the water depth is infinitesimally small, the friction source terms calculated from (36) may become excessively large ($\sim 10^{20}$ depending on ε_h), which may exceed the machine floating number precision and generates unexpected machine error that prohibits a converged solution. To effectively avoid this (e.g., to rescale the equation to $\sim 10^{10}$ and avoid any unexpected machine error), a simple technique is implemented herein. The necessary auxiliary variables are firstly defined as

$$\mathbf{U}_i^{n+1}=\mathbf{Q}_i^{n+1}/h_i^{n+1},\ \mathbf{U}_i^n=\mathbf{Q}_i^n/h_i^{n+1},\ \overline{\mathbf{A}}_i^n=\mathbf{A}_i^n/h_i^{n+1} \tag{37}$$

$$\overline{\mathbf{S}}_i^{n+1}=-gn^2(h_i^{n+1})^{-4/3}\mathbf{U}_i^{n+1}|\mathbf{U}_i^{n+1}| \tag{38}$$

Herein h^{n+1} is known following the update of the continuity equation, which is done before solving the momentum equations. A new time-marching equation for the auxiliary variables can be obtained by dividing both sides of (35) by h_i^{n+1}

$$\mathbf{U}_i^{n+1}=\mathbf{U}_i^n+\Delta t(\overline{\mathbf{A}}_i^n+\overline{\mathbf{S}}_i^{n+1}) \tag{39}$$

This is then solved using the Newton-Raphson method and $\mathbf{Q}_i^{n+1}$ can be easily recovered from $\mathbf{U}_i^{n+1}$ using the relationship as defined in (37).

Table 1. Summary of Models Used for Comparison

Model Name	Slope Source Term	Friction Source Term
George	George's Riemann solver	New implicit
HR	Hydrostatic reconstruction method	New implicit
SRM	New surface reconstruction method	New implicit
SRMEXP	New surface reconstruction method	Old implicit
SRMSPLIT	New surface reconstruction method	Fractional splitting

The Newton-Raphson iteration procedure implemented for solving (39) is given as

$$\mathbf{U}^{p+1}=\mathbf{U}^{p}+[\mathbf{I}-\Delta t\mathbf{J}(\mathbf{U}^{p})]^{-1}[\Delta t\overline{\mathbf{S}}(\mathbf{U}^{p})+\Delta t\overline{\mathbf{A}}_{i}^{n}-(\mathbf{U}^{p}-\mathbf{U}_{i}^{n})] \tag{40}$$

with a convergence criteria defined as

$$|\mathbf{U}^{p+1}-\mathbf{U}^{p}|\leq 0.001|\mathbf{U}^{p}| \tag{41}$$

where $\mathbf{I}$ is the identity matrix, $\mathbf{J}$ is the Jacobian matrix of $\overline{\mathbf{S}}$, p and $p+1$ denote the iteration steps, and $\mathbf{U}_i^n$ provides the initial values to start the iterations. The solution procedure usually converges in two to three steps, or less if the flow is near to a steady state or the friction is small. Numerical experiments show that the iteration procedure requires less than 10% of the run time needed for calculating interface fluxes. Therefore, the current implicit friction term discretization method does not affect the computational efficiency of the overall numerical scheme.

It should be noted that no special treatment is needed for wet-dry front except for assuming a cell is dry and setting the velocities to zero when water depth is smaller than a small threshold (e.g., 10^{-10} m as used in this work).

4.4. Stability Criteria

The proposed fully implicit method for discretizing the friction source terms does not impose any constraint on time steps. The stability criterion for the overall finite volume Godunov-type scheme is therefore the CFL condition, which is given as

$$\Delta t=\mathrm{CFL}\min_{i}\left(\frac{d_i}{|\mathbf{u}_i|+\sqrt{gh_i}}\right) \tag{42}$$

where d_i is the minimum distance from cell center to cell edges and the CFL number may take any value between 0 and 1.

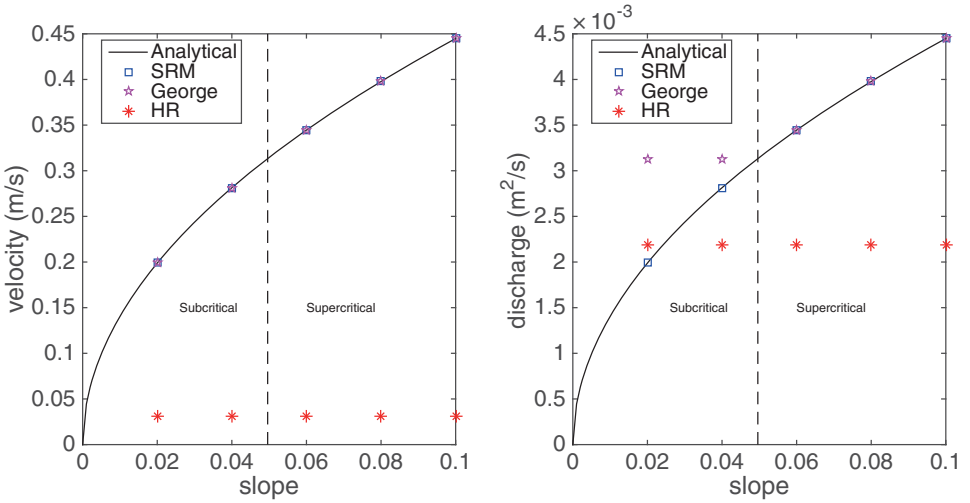

Figure 5. 1-D steady and uniform flow on slopes: computed steady state velocities and discharges on five different slopes. (left) Velocity and (right) discharge.

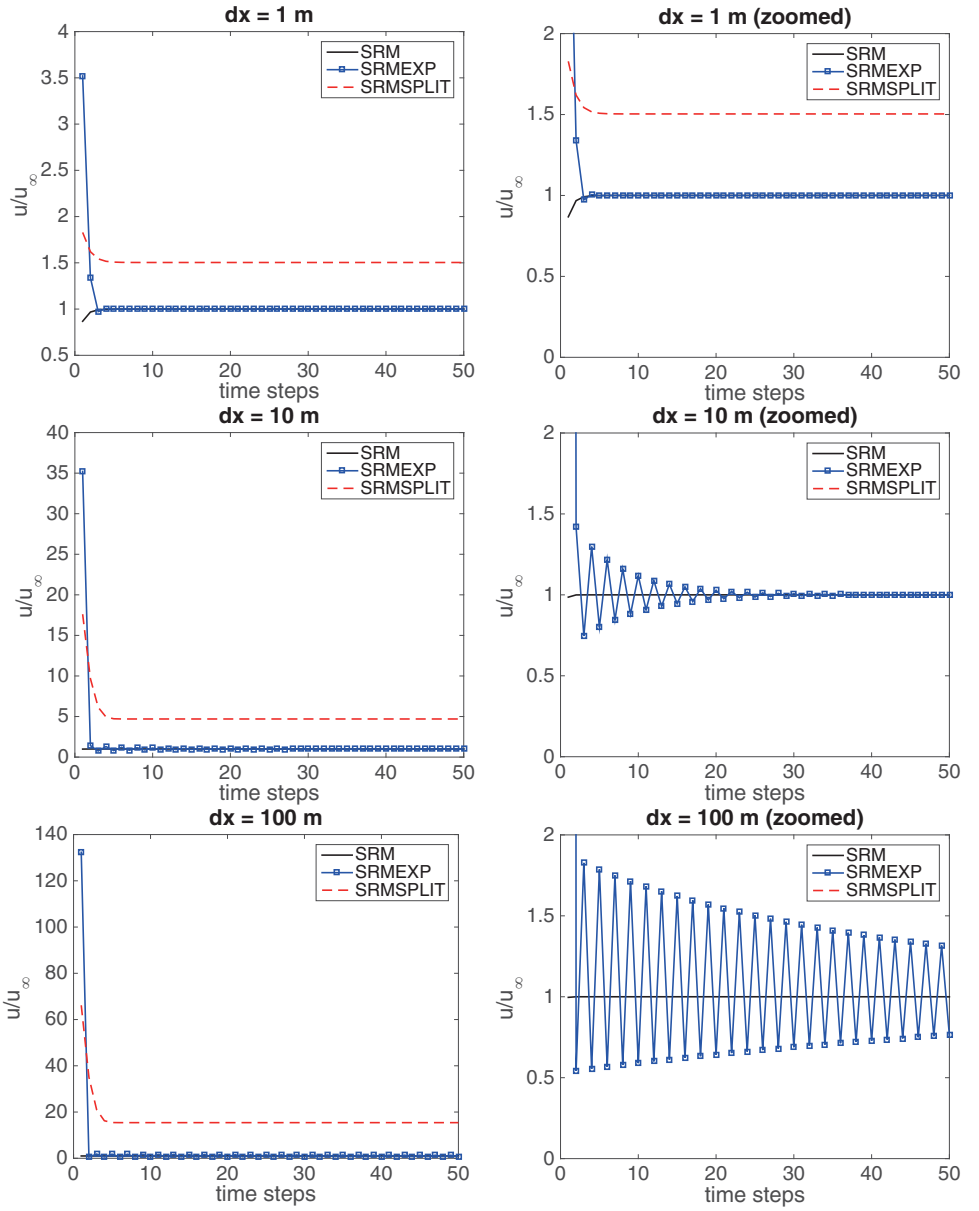

Figure 6. 1-D steady and uniform flow on slopes: relaxation toward the equilibrium state with three different spatial resolutions. (left column) Normal view and (right column) zoomed view for clear illustration of SRM and SRMEXP.

5. Model Validation and Results

In this section, several test cases are simulated to validate the current overland flow model implemented with the proposed novel SRM and implicit friction term discretization scheme. Results obtained from a selection of alternative models introduced in section 3 are compared to demonstrate the improved capability of the current model. Table 1 provides a list of the models used in the simulations with different combinations of slope and friction source term discretization approaches. In Table 1, the old implicit scheme refer to the 2-D form of the explicit reformulation presented in (13) and (14) [e.g., *Song et al.*, 2011a] and the fractional splitting scheme refer to the implicit method used in *Liang and Marche* [2009] for which the 1-D form is presented in (16). In all of the simulations, CFL = 1.0 and $g = 9.81$ m/s^2 are used. The boundary conditions are imposed using the ghost cell method described in *Liang* [2010].

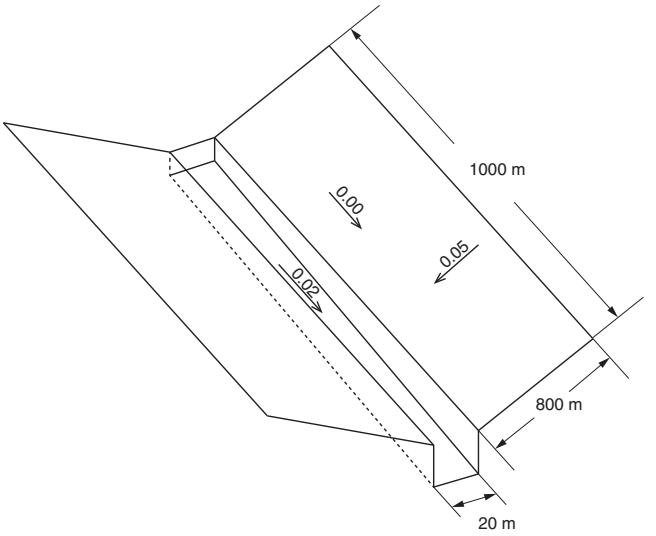

Figure 7. Rainfall on a V-shaped catchment: geometry of the catchment.

5.1. 1-D Steady and Uniform Flow on Slopes

One-dimensional steady and uniform flow on inclined slopes can serve as a basic benchmark test to verify whether the slope source terms and friction source terms are correctly discretized and computed. In this test case, water depth $h = 0.01$ m, the Manning coefficient $n = 0.033$ s m$^{-1/3}$, and five different slopes (0.02, 0.04, 0.06, 0.08, and 0.1) are used. Simulations are carried out at the same spatial resolution ($\Delta x = 10$ m) using models with different schemes to discretize slope source terms. As the slope increases, the steady uniform flow changes from subcritical to supercritical. The steady state velocities computed by different models are plotted against the analytical solution in Figure 5. Both of the "SRM" and "George" models predict correct steady state velocities while the "HR" model fails to give correct results for the flows over all five slopes. The velocities predicted by the "HR" model do not vary with the change of the slopes, indicating that the slope gradient approximated in the "HR" model is effectively bounded. The mass flux at a sample cell interface, i.e., discharge, computed by different models is also compared in Figure 5. For the "HR" and "SRM" models, the discharges are given by the mass flux calculated by the HLLC Riemann solver; for the "George" model, the discharge is calculated by (19). It should be noted that the discharge here is not necessarily the same as hu defined at the cell centers. Only the "SRM" model produces correct interface mass flux for all five slopes. The "HR" model completely fails and predicts the same discharge for all five simulations. The predicted discharge is larger than the analytical discharge at one simulation in the subcritical region but smaller than the correct solution in all other four simulations including one for subcritical flow. The discharge predicted by the "HR" model is consistent with the analysis in section A1, which is $\frac{1}{3}hu + \frac{2}{3}h\sqrt{gh}$. The overestimated discharge is caused by the combination of the constrained slope gradient and the "waterfall effect" as implemented in the numerical scheme. George's augmented Riemann solver overestimates the discharge in the two simulations in the subcritical region, which is consistent with the analysis provided in section 3. Section A2 analytically shows

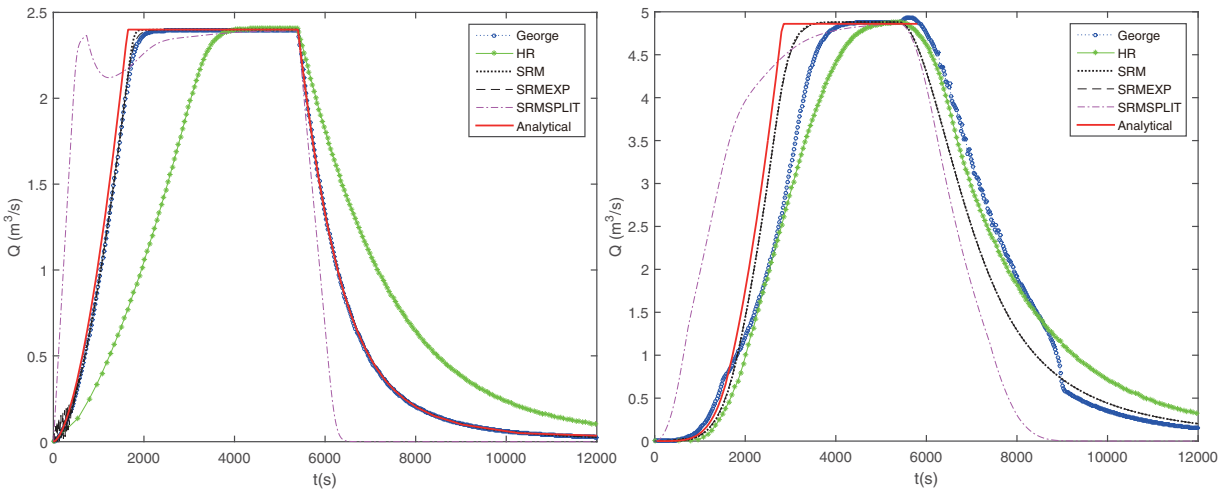

Figure 8. Rainfall on a V-shaped catchment: comparison between the kinematic wave analytical solutions and simulated hydrographs at the (left) hillside and (right) channel outlet. Note that the kinematic wave solution for the falling limb of the channel outlet hydrograph is not available.

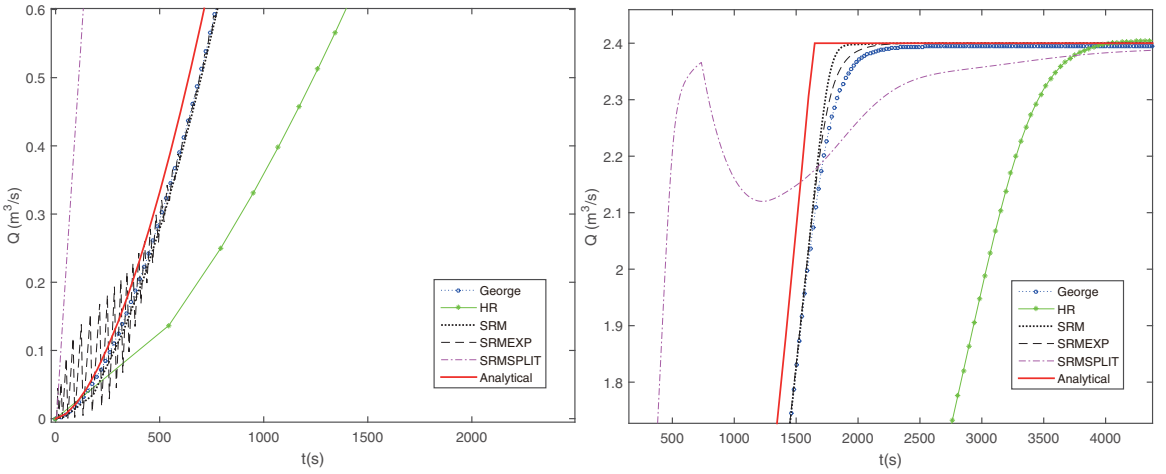

Figure 9. Rainfall on a V-shaped catchment: zoomed-in view of the discharge at the hillside. (left) Initial stage and (right) transition between increasing phase and steady phase.

that the discharge will be $h\sqrt{gh}$ if the depth is smaller than half the bed elevation difference. The discharge computed by the "George" model is therefore consistent with the analysis in section A2.

Further simulations are also carried out using the models with different discretization schemes for the friction source terms to test their capability in terms of relaxing the flow to the equilibrium state. While the time steps predicted by the CFL condition increases with the cell size, the relaxation time toward equilibrium does not depend on the cell size. Therefore, it can be expected that the flow is more likely to be relaxed to the equilibrium state in a single time step when using coarser grids. Therefore, the simulations are performed at three spatial resolution (Δx=1 m, Δx=10 m, and Δx=100 m) and for the same slope (0.1). The water is set as motionless at the beginning. The velocities are normalized by the steady state velocity and plotted against the time step count in Figure 6. The ratios between the relaxation time scale and the hydrodynamic time scale are 0.179, 0.0179, and 0.00179, respectively, for three different grids. This indicates that the relaxation time scales are much smaller than the hydrodynamic time scales and a viable numerical scheme must be able to relax the velocities to the equilibrium in almost a single time step. Clearly, the "SRMSPLIT" model is not able to relax to the correct equilibrium state at all three spatial resolutions and the deviation increases as the resolution decreases. "SRMEXP" can relax the flow to the correct equilibrium state but strong oscillations are observed for coarse grids (Δx=10 m and Δx=100 m). Furthermore, excessively large velocities are observed at the first time step. The reason is that these two schemes are essentially explicit, which effectively results in zero friction at the first time step, leading to large velocities. On the contrary, the "SRM" model with the new friction discretization scheme is able to quickly and monotonically

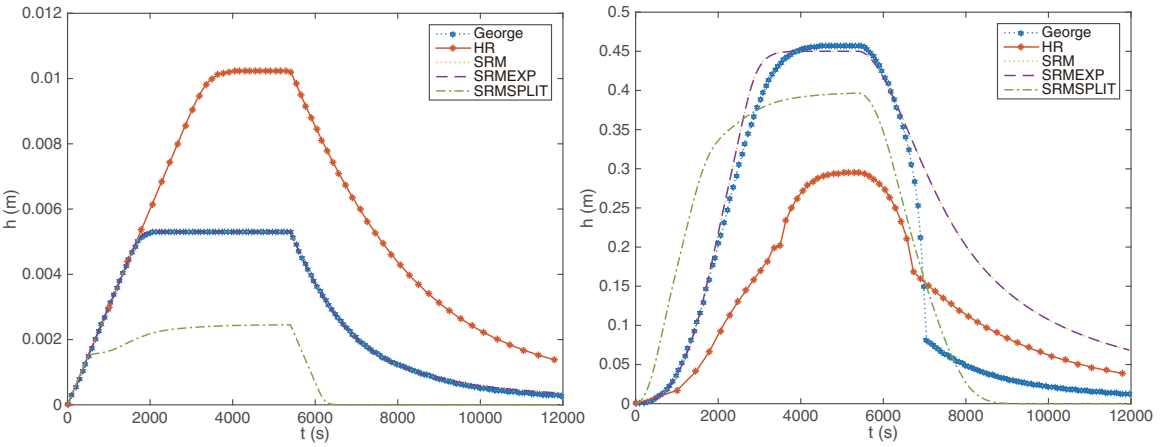

Figure 10. Rainfall on a V-shaped catchment: comparison of time histories of water depth at (left) middle of the hillside end and (right) channel outlet.

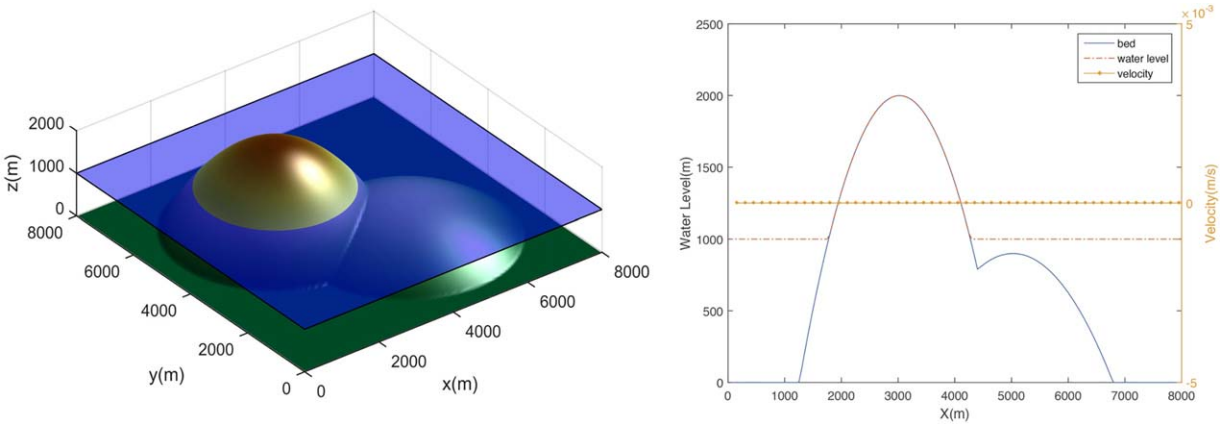

Figure 11. Results for still water test after $t = 5000$ s. (left) 3-D view and (right) water level and velocity at the diagonal cross section.

relax the flow to the correct equilibrium state, achieved in only a single time step even when coarse grids are used ($\Delta x = 10$ m and $\Delta x = 100$ m).

5.2. Rainfall on a V-Shaped Catchment

As shown in Figure 7, the V-shaped catchment consists of two hillsides with a 0.05 slope and, in between, a channel with a 0.02 slope. Constant and uniform rainfall with an intensity of 10.8 mm/h falls on the whole catchment for 1.5 h. The Manning coefficient is set to 0.015 s $m^{-1/3}$ on the hillsides and 0.15 s $m^{-1/3}$ in the channel. During the simulations, the catchment is discretized using a uniform grid of 10 m resolution. The whole domain is closed except for the channel outlet where open boundary conditions are imposed.

Figures 8 and 9 plot the hydrographs at the hillsides and channel outlet predicted by the three different models, comparing with the analytical solutions derived based on the kinematic wave assumption [*Di Giammarco et al.*, 1996]. The time histories of water depth at the middle of hillside end and channel outlet are compared in Figure 10. Closest agreement with the analytical solutions is achieved by the "SRM" model. The hydrographs predicted by the "HR" model has slower rising limbs, which implies that the discharge has been underestimated. The maximum water depth computed by the "HR" model is about 0.01 m, which is much smaller than the bed elevation change across two cells (0.5 m). Therefore, we can conclude that the error is caused by the incorrect approximation of the slope gradient. George's Riemann solver gives a correct hillside hydrograph because the flow is on the hillside is supercritical and George's scheme does not cause an overestimated discharge in supercritical flow conditions. But much less favorable prediction with small unphysical oscillations is found in the hydrograph at the channel outlet.

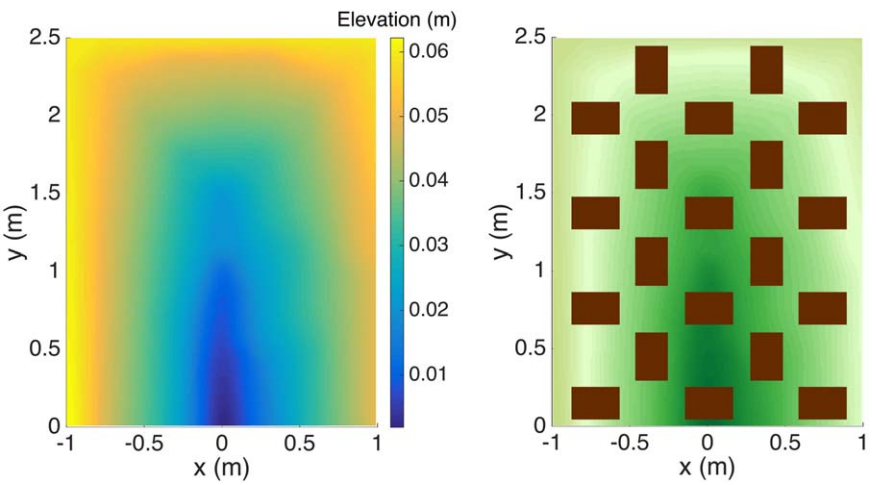

Figure 12. Rainfall-runoff experiment: (left) domain topography and (right) buildings layout.

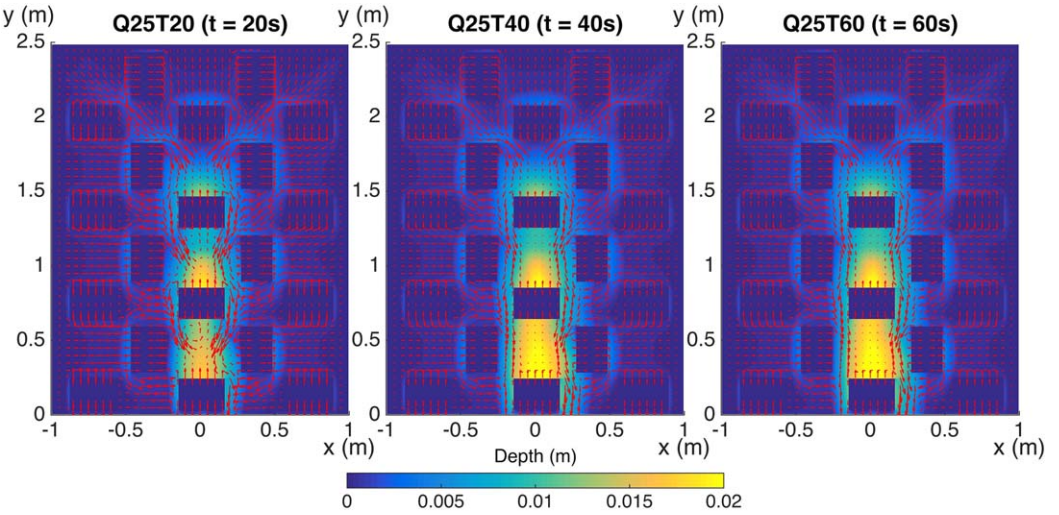

Figure 13. Rainfall-runoff experiment: "SRM" predicted water depths and velocities at the end of the three rainfall events.

With regard to the different friction discretization schemes, the "SRMSPLIT" model gives the worst results. The "SRMEXP" model produces better results; however, unphysical oscillations can be found at the initial stage of the hydrograph at the hillside and larger deviation from the analytical solution is predicted at the rising limb close to the steady phase, as shown in Figure 9. The different results predicted by the models implemented with different friction discretization schemes are consistent with the analysis as provided in section 3 and the results for the 1-D steady uniform flow test. The results clearly confirm that the new friction discretization scheme is indeed able to facilitate accurate and stable simulation of overland flows with reasonable large time steps (CFL = 1.0).

5.3. Still Water Test

In this test case, a quiescent steady flow over uneven topography [*Hou et al*., 2013a] with wet-dry interface is considered to demonstrate that the new "SRM" model is able to preserve the lake at rest solution exactly. The 8000 m × 8000 m domain is discretized into 160 × 160 cells. The topography featured with two overlapped bumps is defined as $b(x,y)=\max(0,B_1,B_2)$ with $B_1=2000-0.00032[(x-3000)^2+(y-5000)^2]$ and $B_2=900-0.000144[(x-5000)^2+(y-3000)^2]$. The initial water level is 1000 m. The simulation results at $t=5000$ s are illustrated in Figure 11 and clearly demonstrate that the lake at rest solution is exactly preserved.

5.4. Rainfall-Runoff Experiment in a Simplified Urban Area

The rainfall-runoff experiment carried out by *Cea et al*. [2010] is considered to further validate the current SWE model for overland flow simulation in urban areas. The experimental urban catchment is represented

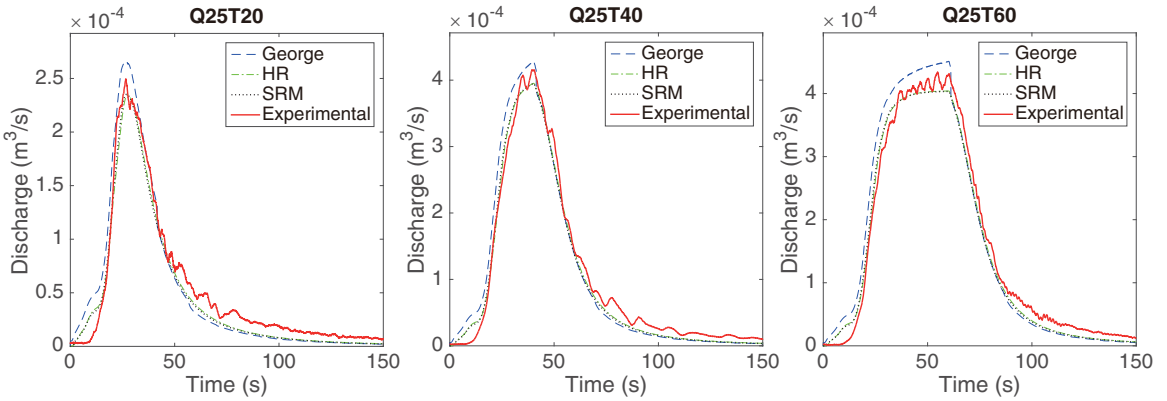

Figure 14. Rainfall-runoff experiment: comparison between the numerical and experimental hydrographs at the domain outlet for the three rainfall events.

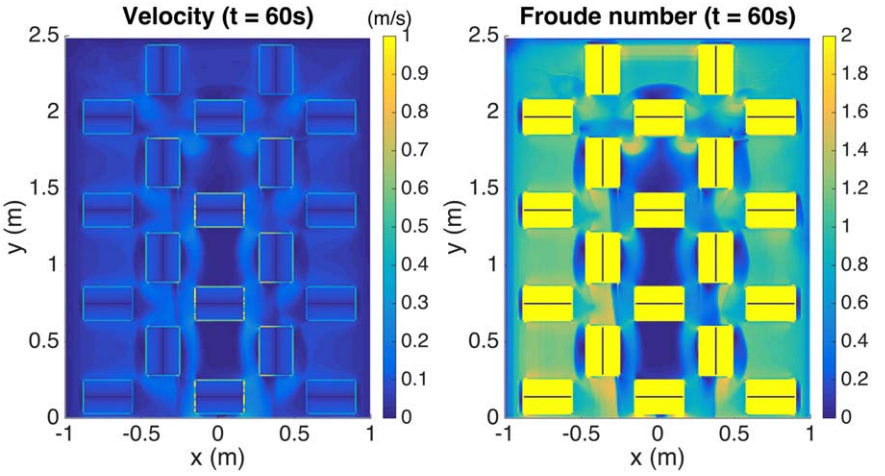

Figure 15. Rainfall-runoff experiment: simulation results predicted by the model implemented with the George's Riemann solver for rainfall event Q25T60 at $t = 60$ s. (left) Velocity and (right) Froude number.

by a steel basin decorated with buildings made from wood blocks, with the topography and the layout of buildings shown in Figure 12. The basin features a valley in the middle with the bottom edge designed to be the outlet. The horizontal dimensions of the buildings are 20 cm $\times$ 30 cm and the vertical outer walls are 20 cm in height. All of the buildings also have a roof with two sloping sides from the center to the edge. Rainfall events with a constant intensity of 300 mm/h but three different durations, i.e., 20, 40, and 60 s, are imposed on the basin. Following *Cea et al*. [2010], the three rainfall events are referred to as Q25T20, Q25T40, and Q25T60.

During the simulation, the building blocks are represented in the model as part of the topography without any further special treatment. The Manning coefficient is set to 0.016 s $m^{-1/3}$ over the entire domain as suggested by *Cea et al*. [2010]. The uniform computational grid consists of 50,000 cells with a resolution of 0.01 m. Zero water depth is assumed in the boundary ghost cells at the bottom edge of the domain to represent the outlet boundary conditions while the other three edges are assumed to be closed.

Figure 13 presents the "SRM" predicted water depths and velocities induced by the three rainfall events at the time when the rainfall stops. It is evident that rainfall-runoff process and the resulting flow patterns are closely related to domain topography. The rainwater flows from sloping roofs of the buildings to the ground, which is then directed to valley at the center of the basin and travels toward the bottom outlet. Although the water depths on the building roofs are very small, the velocities are significant and diverge from the central line of the roofs due to the slopes, indicating correct representation of the slope gradients and runoff with small water depth. Because the proposed numerical scheme effectively handles excessive slopes, at the edges of the buildings where abrupt change of the topography occurs, velocities are not significantly larger than other areas. Figure 14 compares the simulated discharges produced by all three different models with the experiment measurements at the bottom outlet for the three rainfall events. Good agreement is achieved by the "SRM" model for all three cases, confirming the model's simulation accuracy, although the peak discharges seem to be slightly underestimated. The

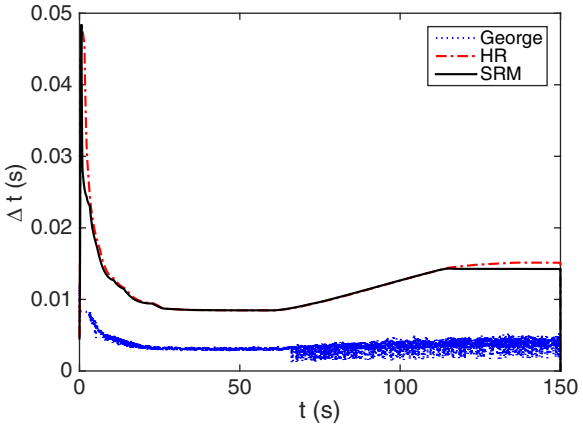

Figure 16. Rainfall-runoff experiment: temporal change of time steps produced by the three different models for the Q25T60 simulations.

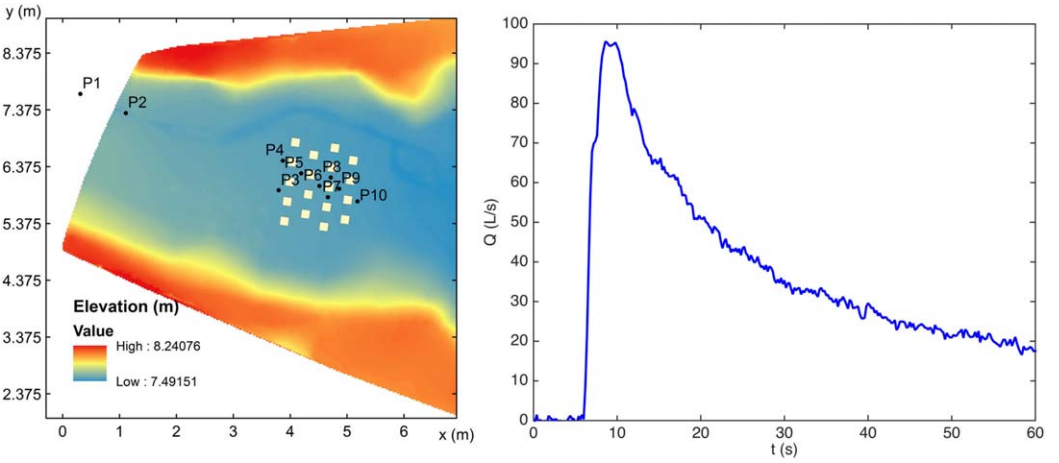

Figure 17. Flash flood onto an urban area: (left) layout of the physical model and (right) inflow hydrograph.

"HR" model also gives good results because the resolution is high for this small-scale test case and the inadequacy of the hydrostatic reconstruction method in handling small water depth is therefore not pronounced. The peak discharges given by the "George" model are slightly larger than the experiments, which may be because the flow in the valley center is mostly subcritical, as illustrated in Figure 15b, and the George's Riemann solver typically overestimates discharge on slopes for subcritical flows as discussed in section 3. It is worth mentioning that the cell size used in this test case is much smaller than that could be used for real-world simulations, so that the limitations of the "HR" and "George" models relating to the inaccurate calculation of slope source terms and discharge are not particularly pronounced and all three methods provide similar results.

In this test, the entire domain is wet due to uniform rainfall events. Because George's Riemann solver does not involve any special treatment to trim the large slopes due to discontinuous bathymetry, the predicted velocities near to building walls where abrupt change of bed elevation occurs are significantly higher (5–10 times) than those in other areas with smooth topography. Such "big" velocities are caused by numerical rather than physical reasons. In reality, the water gains momentum when falling off a roof, but most of the gained momentum is in the vertical direction and will be dissipated when water hits the ground, which does not necessarily lead to the increase of horizontal velocities. However, these "big" velocities effectively control the model stability, leading to the use of much smaller time steps, as shown in Figure 16. This inevitably affects the computational efficiency of the model.

5.5. Laboratory-Scale Flash Flood Onto a Simplified Urban District

This urban flash flood experiment was carried out by *Testa et al*. [2007] as part of the joint European IMPACT (Investigation of extreMe flood Processes And unCerTainty) project. The physical model is a 1:100 representation of the Toce River valley built in the CESI facility in Milan, Italy. Cubic concrete blocks with a side length of 15 cm were placed in a staggered layout to represent buildings, as shown in Figure 17. The inflow hydrograph (total discharge at the inlet), as shown in Figure 17, was controlled by a head tank located at the left-hand side of the valley [*Testa et al*., 2007], which was referred to as the "low" discharge in *Testa et al*. [2007]. The water depth was continuously measured at 10 gauge points during the 60 s of the experiment; the locations of the gauges are also illustrated in Figure 17. Open boundary conditions are imposed at the downstream (right) end of the valley.

The Manning coefficient is set to 0.0162 s $m^{-1/3}$ as suggested by *Testa et al*. [2007]. A uniform computational grid at a 0.025 m $\times$ 0.025 m resolution is used for the simulation. The buildings are represented in the models by simply raising the bed elevation 0.15 m above the ground. Figure 18 presents the "SRM" predicted water depths and velocities at different output times, which clearly shows the model's capability in capturing the transient features of the flash flood. The velocity of the flood front is high before it reaches the buildings; the flow is then slowed down

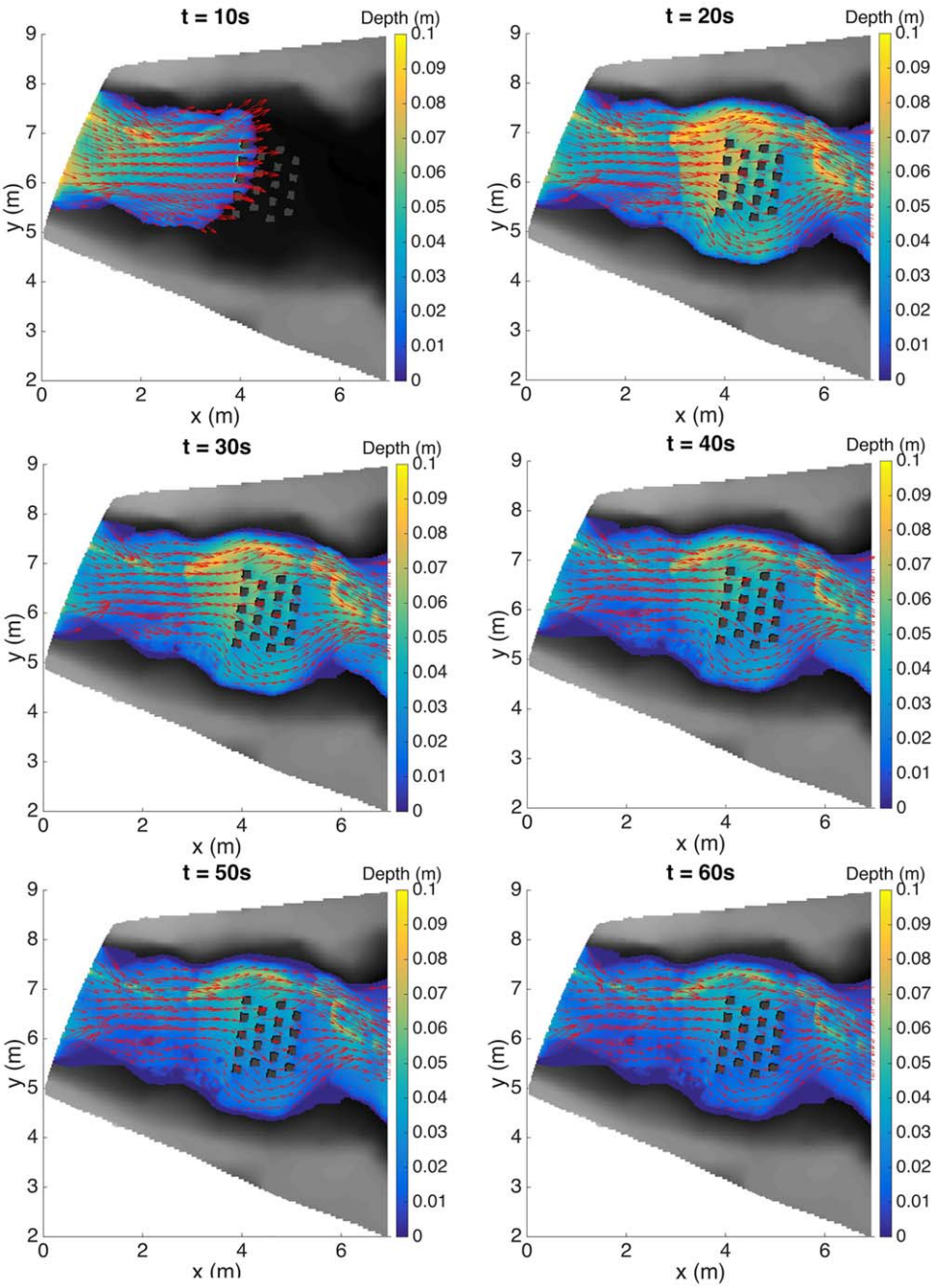

Figure 18. Flash flood onto an urban area: simulated water depths and velocities.

by the buildings and a reflected shock is developed. Meanwhile, a significant amount of floodwater bypasses the built area through the two sides of the valley. Flood depth starts to decrease after the peak flow has passed. Figure 19 further verifies the current simulation results by comparing the predicted time histories of water depth with the measured data and those predicted by alternative models ("George" and "HR"). Overall, the current numerical results agree well with the measurements and correctly predict both of the arriving time and peak water depth except for Gauges P6 and P8, where the numerical simulation underestimates the flood peak by 1 and 2 cm, respectively. This may be attributed to the three-dimensional flow phenomena associated with this highly transient and turbulent flow processes that are not able to be captured by the

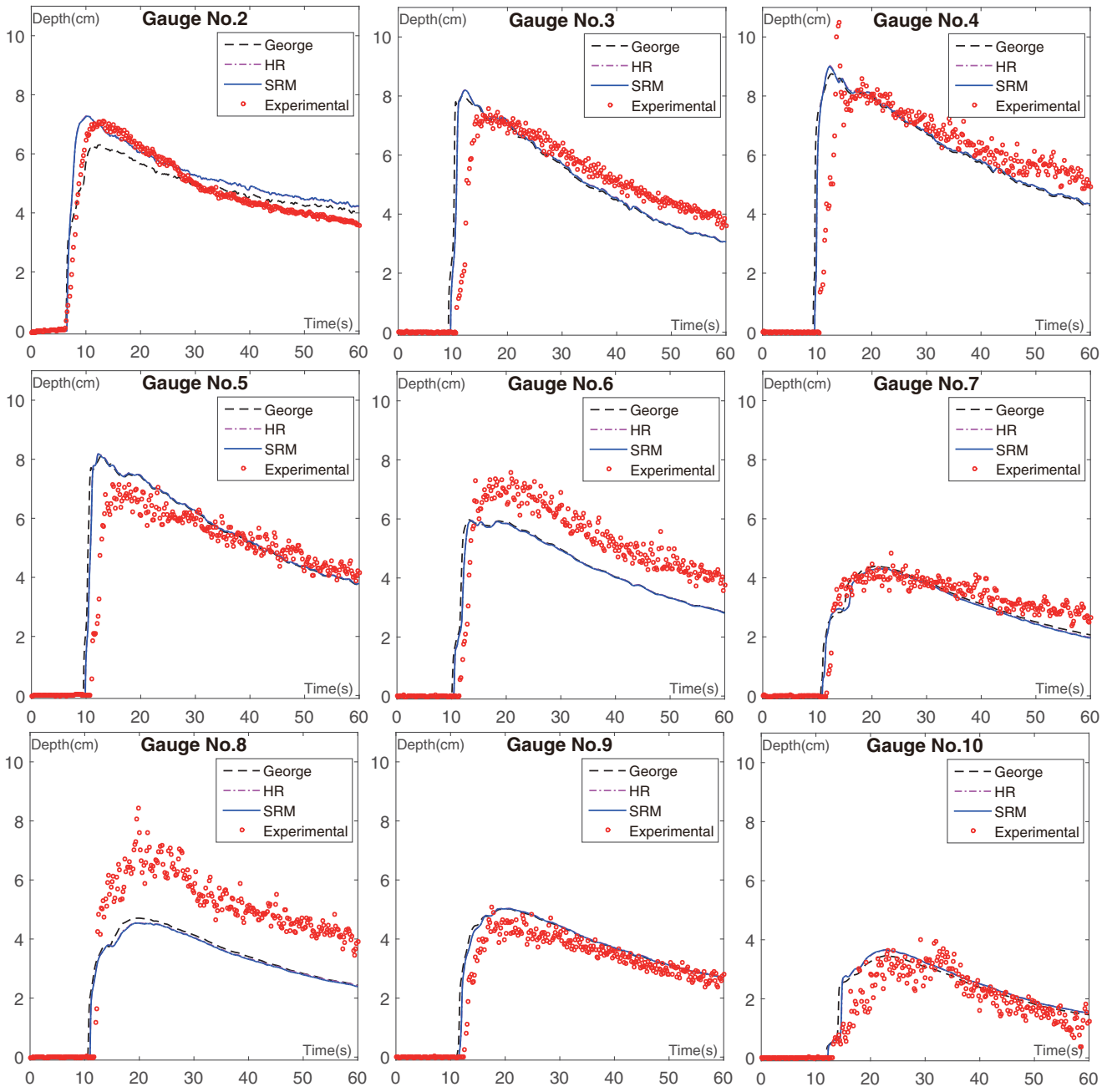

Figure 19. Flash flood onto an urban area: time histories of water depth at nine sample gauges.

shallow water equations. Satisfactory reproduction of this experimental benchmark test confirms that the current SRM model can successfully simulate those highly transient flows with wetting and drying. This test case does not typically involve those challenging perspectives for overland flow simulations, and so most Godunov-type schemes can produce satisfactory results. The results predicted by the "SRM" model are similar to the alternative simulations produced by the other two models.

5.6. Hypothetic Rainfall Event on the Haltwhistle Burn Catchment

The Haltwhistle Burn catchment, covering an area of about 42 km^2, is a small catchment in Northumberland, England. It is one of the Rapid Response Catchments recognized by the UK Environment Agency. The topographic map of the catchment is shown in Figure 20.

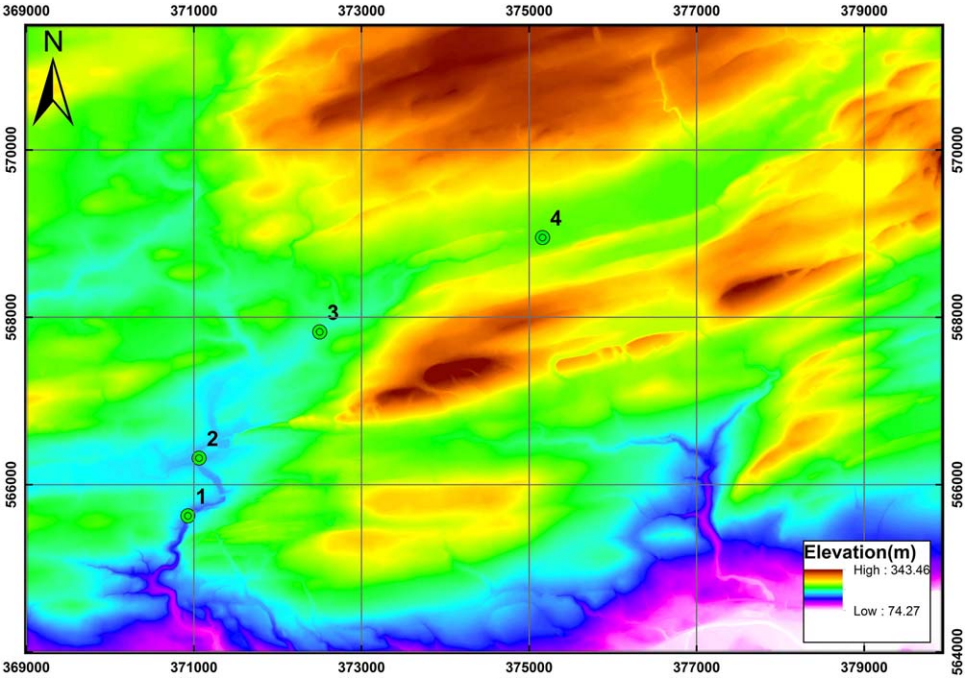

Figure 20. The topographic map of the Haltwhistle Burn catchment and the locations of the gauges.

In order to verify the new model's capability in simulating overland flows over real-world topography, a hypothetic rainfall event is assumed and the resulting rainfall-runoff and overland flow processes are simulated using the new SRM model. Constant and uniform rainfall with an intensity of 45 mm/h is assumed to

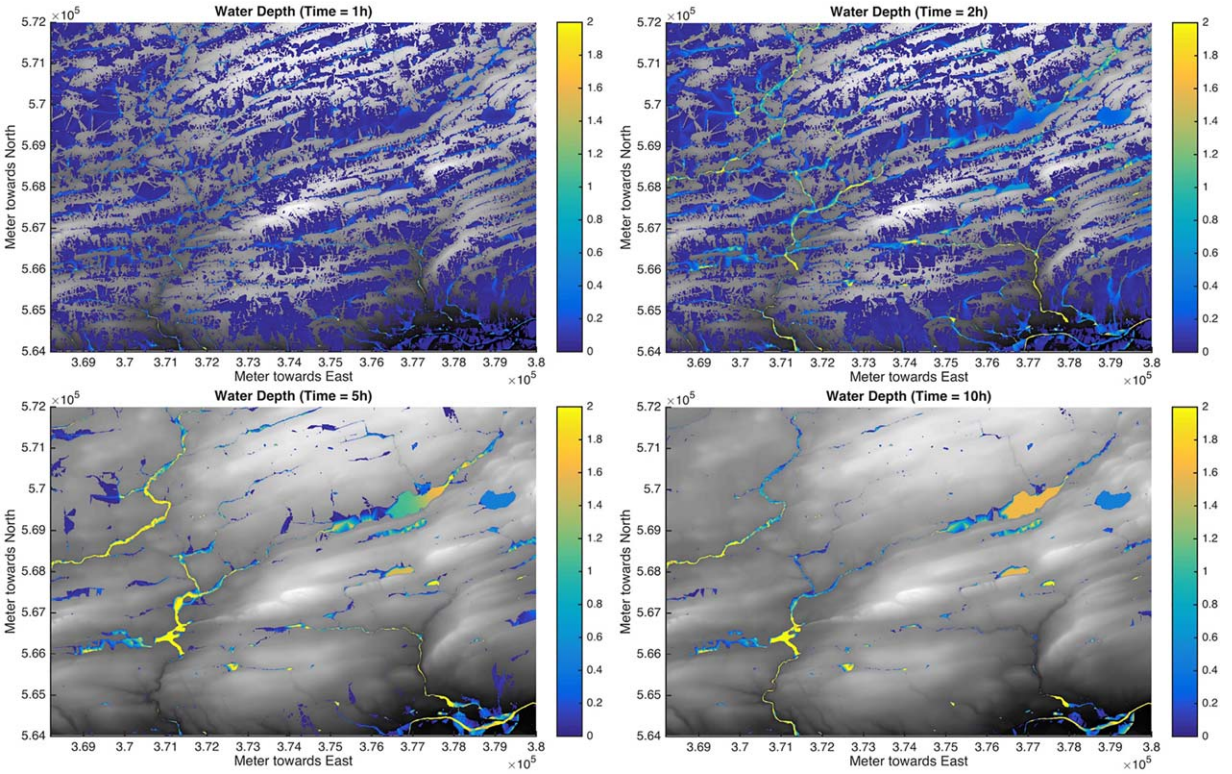

Figure 21. Hypothetic rainfall event on the Haltwhistle Burn catchment: water depth (in meters) predicted by the new model at $t = 1$ h, $t = 2$ h, $t = 5$ h, and $t = 10$ h.

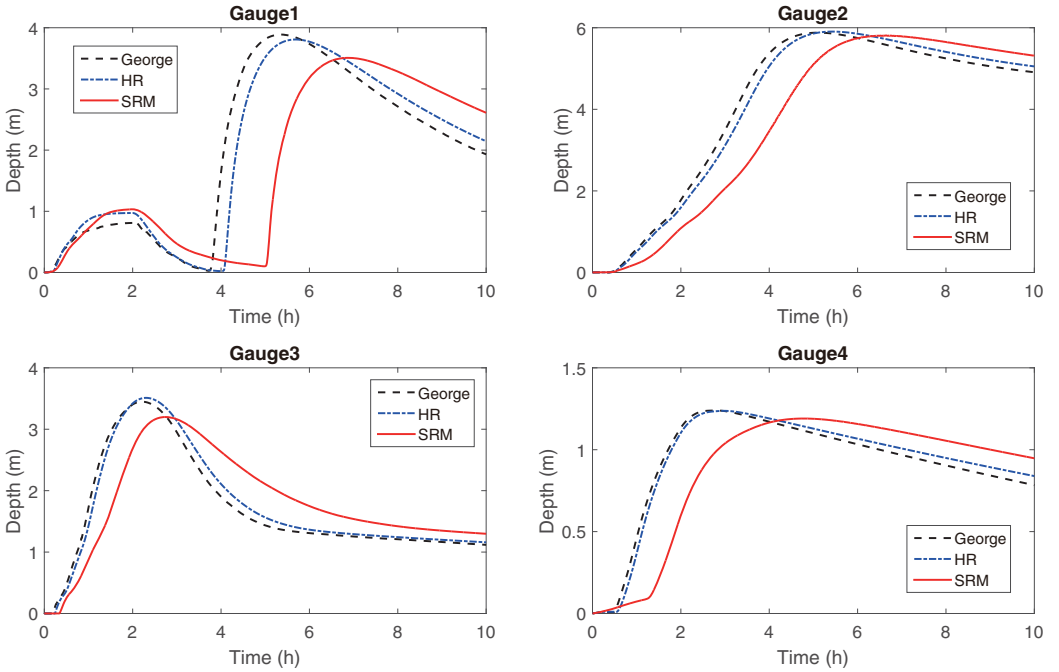

Figure 22. Hypothetic rainfall event on the Haltwhistle Burn catchment: time histories of water depth at the four gauges.

fall on the whole catchment for 2 h. The simulation is carried out for a total of 10 h starting from the beginning of the rainfall. Most of the catchment is covered by pastures and so a constant Manning coefficient of 0.05 s $m^{-1/3}$ is used. Zero infiltration is assumed and open boundary conditions are imposed. The rectangular computational domain embracing the catchment is discretized by a uniform grid at a 5 m resolution, leading to 4 million cells. During the simulation, water level is monitored at four gauges located along the Haltwhistle Burn. The water depth simulated by the new "SRM" model is shown in Figure 21. The rainfall-induced overland flow converges into the streams, river channels, and lower parts of the catchment, which is as expected. Figure 22 presents the time histories of water depth recorded at the four gauges. In order to compare numerical results, simulations are also carried out using alternative models (i.e., "George" and "HR"). From the results, it is observed that "George" and "HR" perform more consistently than the SRM model and both predict earlier arrival of the flood peaks. To better explain this, the Froude number of the flow predicted by the "George" model is plotted in Figure 23 for $t = 2$ h. The Froude number is relatively small in almost the entire domain and the flow is predominantly subcritical. It has been concluded that George's Riemann solver tends to overestimate the discharge on slopes when the flow is subcritical and this obviously explains the earlier arrival of flood peaks. The early arrival of flood peaks predicted by the "HR" model may be explained by the overestimated discharge caused by the "waterfall effect" in this case. The cell size used in the simulation is 5 m and the water depth on the slopes is typically at an order of 0.01 m. As a result, even a gentle slope can lead to variation of bed elevation between neighboring cells larger than the water depth,

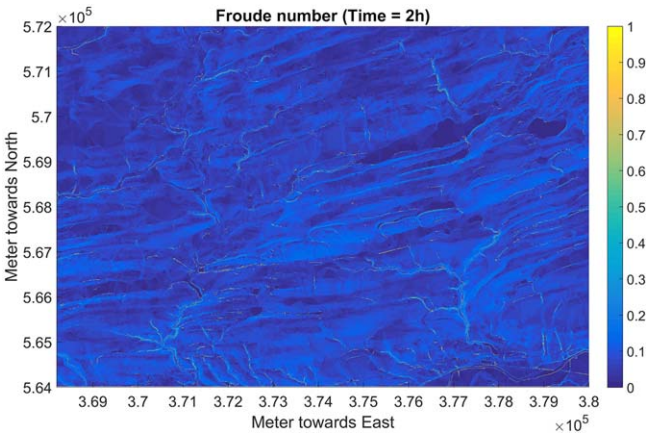

Figure 23. Haltwhistle hypothetic flood: Froude number predicted by the model with George's Riemann solver at $t = 2$ h.

Table 2. Hypothetic Rainfall Event on the Haltwhistle Burn Catchment: Time Steps Count and Total Run Time for Three Simulations

Model Name	Time Steps Count	Total Run Time (min)
George	154,744	595
HR	151,034	137
SRM	151,089	199

effectively causing the "waterfall effect." The "SRM" model as presented does not suffer from either of these limitations and hence predicts later arrival of the flood peaks. It is interesting to notice that "George" and "HR" models give similar results although they both suffer from certain limitations for overland flow simulations. In Appendix A, it is shown that for the simple steady flow with uniform depth and velocity, the discharge given by the "HR" model is $\frac{1}{3}hu+\frac{2}{3}h\sqrt{gh}$. The discharge given by the "George" model is $h\sqrt{gh}$ if $h < 1/2\times b_i - b_{i+1}$ is true, which is most likely the case in this test. The difference between $\frac{1}{3}hu+\frac{2}{3}h\sqrt{gh}$ and $h\sqrt{gh}$ is indeed much smaller than the difference between $h\sqrt{gh}$ and the true discharge hu. Although the analysis is rudimentary, the results in Figure 22 are qualitatively in line with the mathematical analysis.

In order to compare their computational efficiency, the three different models are implemented in the same GPU-accelerated code base and simulations are all carried out on a NVIDIA Tesla K40 GPU. Table 2 provides the quantitative comparison of the time step count and run time required by the three models. The three different simulations need similar number of time steps to finish the whole simulation. Unlike the urban rainfall experiment test previously considered, the "George" model does not require much more time steps than the other two models because the time steps are more controlled by the largest water depth in the river channels rather than the flow velocity for this specific case. In terms of run time, the new "SRM" model consumes 199 min to finish the 10 h simulation, about 40% more than the 137 min as required by the "HR" model. The computational efficiency between the two models is therefore comparable and the new SRM implementation does not necessarily lead to substantial increase of computational cost. On the other hand, the "George" model is found to be nearly 3 times slower than the current SRM model due to the complexity of the Riemann solver.

6. Conclusion

This paper discusses in detail the existing challenges encountered in overland flow simulations and proposes new discretization schemes to deal with these challenges, and subsequently implement these new schemes to devise a hydrodynamic overland flow model with much improved numerical accuracy and stability, as well as computational efficiency. The improved model has the following key features:

1. Through implementation of a novel surface reconstruction method (SRM), the current hydrodynamic overland flow model is able to correctly compute the bed slope source terms in the limit of disappearing water depth, maintain numerical stability for simulations over rough terrains with abrupt change of bed profiles, and preserve the lake at rest solution with wetting and drying.
2. An implicit scheme is proposed to discretize the strongly nonlinear friction source terms, allowing correct recovery of the theoretical equilibrium state of the shallow flows when water depth is small and friction becomes dominant. This new implicit friction discretization scheme allows accurate and stable simulations using "normal" time steps controlled by the CFL condition, effectively improving computational efficiency.
3. When incorporating with a classic Riemann solver solving the homogeneous SWEs (e.g., the HLLC approximate Riemann solver as adopted in this work), the new model is able to give correct prediction of mass flux, i.e., unit discharge, on slopes in the limit of disappearing water depth.

These features are essential for accurate, stable, and efficient simulation of overland flows and flash floods which usually involves very shallow water flowing downhill. Theoretical analysis and numerical simulations show that certain models solving the SWEs, such as the hydrostatic reconstruction scheme [*Audusse et al.*, 2004] and the augmented Riemann solver [*George*, 2008], are not simultaneously equipped with all these numerical features and therefore may not be able to accurately simulate overland flows.

The overland flow and surface flood model developed in this work resolves the aforementioned numerical challenges and has all of the above positive features in a single code base. The model is validated against several test cases and produced numerical results that agree closely with analytical solutions or

experimental measurements. The stability and efficiency of the current model has been further demonstrated by simulating a hypothetic rainfall event in the Haltwhistle Burn catchment.

The proposed new discretization schemes are easy to implement and independent of the Riemann solver being used and provide great flexibility for the users to develop or improve their own models. Although the current model is developed and tested on uniform Cartesian grids, the overall mathematical and numerical framework is compatible with and can be extended readily to other types of grids, e.g., unstructured grids.

Appendix A: Overestimation of Mass Flux by Hydrostatic Reconstruction and George's Riemann Solver

A1. Overestimation of Mass Flux Due to the "Waterfall" Effect

In this paper, the HLLC Riemann solver [*Toro*, 2001] is adopted, which is summarized as below. Taking the x direction flux $\mathbf{f}$ as an example, the HLLC Riemann solver gives

$$\mathbf{f}=\begin{cases}\mathbf{f}_L & 0\le S_L\\ \mathbf{f}_{*L} & S_L\le 0\le S_M\\ \mathbf{f}_{*R} & S_M\le 0\le S_R\\ \mathbf{f}_R & S_R\le 0\end{cases} \tag{A1}$$

in which $\mathbf{f}_L=\mathbf{f}(\mathbf{q}_L)$ and $\mathbf{f}_R=\mathbf{f}(\mathbf{q}_R)$ are calculated from the left and right Riemann states and S_L, S_R, and S_M the are characteristic wave speeds. $\mathbf{f}_{*L}$ and $\mathbf{f}_{*R}$ are the fluxes in the left and right middle regions of the HLLC solution structure, calculated as

$$\mathbf{f}_{*L}=\begin{bmatrix}f_{*1}\\ f_{*2}\\ v_L f_{*1}\end{bmatrix}\quad \mathbf{f}_{*R}=\begin{bmatrix}f_{*1}\\ f_{*2}\\ v_R f_{*1}\end{bmatrix} \tag{A2}$$

with the HLL fluxes $\mathbf{f}_*$ provided by the following formula

$$\mathbf{f}_*=\frac{S_R\mathbf{f}_L-S_L\mathbf{f}_R+S_LS_R(\mathbf{q}_R-\mathbf{q}_L)}{S_R-S_L} \tag{A3}$$

The formulae for the left and right characteristic wave speeds S_L and S_R are

$$S_L=\begin{cases}u_R-2\sqrt{gh_R} & h_L=0\\ \min(u_L-\sqrt{gh_L},u_*-\sqrt{gh_*}) & h_L>0\end{cases} \tag{A4}$$

$$S_R=\begin{cases}u_L-2\sqrt{gh_L} & h_R=0\\ \max(u_R+\sqrt{gh_R},u_*+\sqrt{gh_*}) & h_R>0\end{cases} \tag{A5}$$

in which

$$u_*=\frac{1}{2}(u_L+u_R)+\sqrt{gh_L}-\sqrt{gh_R} \tag{A6}$$

$$h_*=\frac{1}{g}\left[\frac{1}{2}(\sqrt{gh_L}+\sqrt{gh_R})+\frac{1}{4}(u_L-u_R)\right]^2 \tag{A7}$$

The middle characteristic wave speed S_M is calculated as

$$S_M=\frac{S_Lh_R(u_R-S_R)-S_Rh_L(u_L-S_L)}{h_R(u_R-S_R)-h_L(u_L-S_L)} \tag{A8}$$

We assume that the left-hand side bed elevation is higher than the right-hand side water level at the cell interface under consideration. The left and right Riemann states after hydrostatic reconstruction are (h_L, hu_L) and (0, 0,) respectively. Further assuming that the flow is subcritical, the mass flux given by the HLLC Riemann solver can be obtained as $\frac{1}{3}hu_L+\frac{2}{3}h_L\sqrt{gh_L}$ by substituting the Riemann states into (A1)–(A8).

A2. Overestimation of Mass Flux by George's Riemann Solver in Subcritical Flow Conditions

LeVeque [1997] defined the following relationship between the mass fluctuations and mass fluxes:

$$\mathcal{A}^- \Delta H_{i+1/2} = F^h_{i+1/2} - hu_i \tag{A9}$$

$$\mathcal{A}^+ \Delta H_{i+1/2} = hu_{i+1} - F^h_{i+1/2} \tag{A10}$$

where $F^h_{i+1/2}$ is the mass flux across the cell interface with clear physical meanings, both sides of (A9) and (A10) represent the changing rate of mass at the half-cell $[x_i, x_{i+\frac{1}{2}}]$ and $[x_{i+\frac{1}{2}}, x_i]$, respectively. Then the cell interface mass flux can be expressed by the mass fluctuations as

$$F^h_{i+1/2} = \mathcal{A}^- \Delta H_{i+1/2} + hu_i \tag{A11}$$

or

$$F^h_{i+1/2} = hu_{i+1} - \mathcal{A}^+ \Delta H_{i+1/2} \tag{A12}$$

Both (A11) and (A12) are true because the fluctuations must satisfy

$$\mathcal{A}^- \Delta H_{i+1/2} + \mathcal{A}^+ \Delta H_{i+1/2} = hu_{i+1} - hu_i \tag{A13}$$

to ensure mass conservation [see *George*, 2008]. (A11) and (A12) are also applicable to the augmented Riemann solver in *George* [2008] because no specific form of fluctuations is assumed.

Now we prove that $\mathcal{A}^- \Delta H_{i+1/2} > 0$ providing that the following conditions are satisfied

$$\sqrt{gh} > u > 0 \ , \ h = const \ , \ u = const \ \text{and} \ b_i > b_{i+1} \tag{A14}$$

Proof of the above statement simply needs to follow the solution procedure described in *George* [2008] but requires a substantial amount of algebraic manipulations and is rather lengthy. Therefore, we summarize the key steps here and some of the equations we used here can be found in *George* [2008]. For better reference, from now on we follow the notations as used in *George* [2008].

Proof:

Considering the conditions given in (A14), the following is obviously true

$$\begin{bmatrix} H_{i+1} - H_i \\ HU_{i+1} - HU_i \\ \phi(Q_{i+1}) - \phi(Q_i) \\ B_{i+1} - B_i \end{bmatrix} = \begin{bmatrix} 0 \\ 0 \\ 0 \\ B_{i+1} - B_i \end{bmatrix} \tag{A15}$$

From *George* [2008, equations (35a)–(35c)], we can obtain that

$$\{w^1_{i+1/2}, s^1_{i+1/2}\} = \{(1, U - \sqrt{gH}, (U - \sqrt{gH})^2, 0)^T, U - \sqrt{gH}\} \tag{A16}$$

$$\{w^2_{i+1/2}, s^2_{i+1/2}\} = \{(0, 0, 1, 0)^T, U\} \tag{A17}$$

$$\{w^3_{i+1/2}, s^3_{i+1/2}\} = \{(1, U + \sqrt{gH}, (U + \sqrt{gH})^2, 0)^T, U + \sqrt{gH}\} \tag{A18}$$

$s^0_{i+1/2}$ is always 0. For $w^0_{i+1/2}$, there are two possibilities: the first possibility is that $(w^0_{i+1/2})^1$ calculated from *George* [2008, equation (41)] reaches the lower bound in *George* [2008, equation (49)] (note that the upper bound is always satisfied in our condition). Then the following is obtained

$$w^0_{i+1/2} = \left(\frac{2H\sqrt{gH}}{(U + \sqrt{gH})(B_{i+1} - B_i)}, 0, -gH, 1\right)^T \tag{A19}$$

Another possibility is that $(w^0_{i+1/2})^1$ calculated from *George* [2008, equation (41)] does not reach the lower bound in *George* [2008, equation (49)]. Then we can obtain that

$$w^0_{i+1/2} = \left(\frac{gH}{U^2 - gH}, 0, -gH, 1\right)^T \tag{A20}$$

If (A19) is true, after solving the matrix in *George* [2008, equation (29)], which reads

$$\begin{bmatrix} H_{i+1}-H_i \\ HU_{i+1}-HU_i \\ \phi(Q_{i+1})-\phi(Q_i) \\ B_{i+1}-B_i \end{bmatrix} = \sum_{p=0}^{3} \alpha_{i+1/2}^{p} w_{i+1/2}^{p} \tag{A21}$$

we can obtain

$$\begin{bmatrix} \alpha_{i+1/2}^{0} \\ \alpha_{i+1/2}^{1} \\ \alpha_{i+1/2}^{2} \\ \alpha_{i+1/2}^{3} \end{bmatrix} = \begin{bmatrix} B_{i+1}-B_i \\ -H \\ 2H\sqrt{gH}(\sqrt{gH}-U)+(B_{i+1}-B_i)gH \\ \dfrac{H(U-\sqrt{gH})}{U+\sqrt{gH}} \end{bmatrix} \tag{A22}$$

After applying *George* [2008, equation (30), equation (23a)], which respectively reads

$$\mathcal{Z}_{i+1/2}^{p} = [\mathbf{0}_{2\times 1} \ \ \mathbf{I}_{2\times 2} \ \ \mathbf{0}_{2\times 1}] \alpha_{i+1/2}^{p} w_{i+1/2}^{p} \tag{A23}$$

and

$$\mathcal{A}^{-}\Delta Q_{1+1/2} = \sum_{p:s_{i+1/2}^{p}<0} \mathcal{Z}_{i+1/2}^{p} \tag{A24}$$

we can obtain

$$\mathcal{A}^{-}\Delta Q_{1+1/2} = \{H(\sqrt{gH}-U), -H(\sqrt{gH}-U)^2\}^T \tag{A25}$$

Similarly, if (A20) is true, we can obtain

$$\mathcal{A}^{-}\Delta Q_{1+1/2} = \{-\frac{1}{2}(B_{i+1}-B_i)\sqrt{gH}, -\frac{1}{2}(B_{i+1}-B_i)(U-\sqrt{gH})\sqrt{gH}\}^T \tag{A26}$$

In both cases, it is trivial to prove that the first component of $\mathcal{A}^{-}\Delta Q_{1+1/2}$, i.e., $\mathcal{A}^{-}\Delta H_{1+1/2}$ is positive. We may also prove that $\mathcal{A}^{-}\Delta H_{1+1/2}$ is always the smallest possible value between (A25) and (A26). Consequently, $\mathcal{A}^{-}\Delta H_{1+1/2}$ is always the value given in (A25) if

$$H < \frac{1}{2}(B_i - B_{i+1}) \tag{A27}$$

In such a condition, the mass flux across the cell interface is $H(\sqrt{gH}-U)+HU=H\sqrt{gH}$, which is close to the mass flux predicted by the hydrostatic reconstruction method in the presence of the "waterfall effect." It is also noteworthy that (A27) is similar to the condition under which the "waterfall effect" occurs.

Acknowledgments
This work is funded by the NERC SINATRA and TENDERLY projects (grant NE/K008781/1) and REMATCH project (grant NE/P015476/1). The authors thank Luis Cea (e-mail address: luis.cea@udc.es) for providing the experimental data for the rainfall-runoff experiment in a simplified urban area. The DEM of the Haltwhistle catchment is obtained from Digimap (http://digimap.edina.ac.uk). The authors also thank four anonymous reviewers for their constructive comments, which have helped improve substantially the paper.

References

Audusse, E., F. Bouchut, M.-O. Bristeau, R. Klein, and B. Perthame (2004), A fast and stable well-balanced scheme with hydrostatic reconstruction for shallow water flows, *SIAM J. Sci. Comput.*, *25*(6), 2050–2065, doi:10.1137/S1064827503431090.

Bates, P. D., M. S. Horritt, and T. J. Fewtrell (2010), A simple inertial formulation of the shallow water equations for efficient two-dimensional flood inundation modelling, *J. Hydrol.*, *387*(1–2), 33–45, doi:10.1016/j.jhydrol.2010.03.027.

Berger, M. J., D. L. George, R. J. LeVeque, and K. T. Mandli (2011), The GeoClaw software for depth-averaged flows with adaptive refinement, *Adv. Water Resour.*, *34*(9), 1195–1206, doi:10.1016/j.advwatres.2011.02.016.

Bermúdez, A., A. Dervieux, J.-A. Desideri, and M. Vázquez (1998), Upwind schemes for the two-dimensional shallow water equations with variable depth using unstructured meshes, *Comput. Methods Appl. Mech. Eng.*, *155*(1), 49–72, doi:10.1016/S0045-7825(97)85625-3.

Bouchut, F., and T. de Luna (2010), A subsonic-well-balanced reconstruction scheme for shallow water flows, *SIAM J. Numer. Anal.*, *48*(5), 1733–1758, doi:10.1137/090758416.

Burguete, J., P. García-Navarro, and J. Murillo (2008), Friction term discretization and limitation to preserve stability and conservation in the 1D shallow-water model: Application to unsteady irrigation and river flow, *Int. J. Numer. Methods Fluids*, *58*(4), 403–425, doi:10.1002/fld.1727.

Busaman, A., K. Mekchay, and S. Siripant (2015), Dynamically adaptive tree grid modeling for simulation and visualization of rain-water overland flow, *Int. J. Numer. Methods Fluids*, *79*, 559–579, doi:10.1002/fld.4064.

Caviedes-Voullième, D., P. García-Navarro, and J. Murillo (2012), Influence of mesh structure on 2D full shallow water equations and SCS Curve Number simulation of rainfall/runoff events, *J. Hydrol.*, *448–449*, 39–59, doi:10.1016/j.jhydrol.2012.04.006.

Cea, L., and E. Blade (2015), A simple and efficient unstructured finite volume scheme for solving the shallow water equations in overland flow applications, *Water Resour. Res.*, *51*, 5464–5486, doi:10.1002/2014WR016259.

Cea, L., and M. Vazquez-Cendon (2010), Unstructured finite volume discretization of two-dimensional depth-averaged shallow water equations with porosity, *Int. J. Numer. Methods Fluids*, *63*, 903–930, doi:10.1002/fld.2107.
Cea, L., M. Garrido, and J. Puertas (2010), Experimental validation of two-dimensional depth-averaged models for forecasting rainfall-runoff from precipitation data in urban areas, *J. Hydrol.*, *382*(1–4), 88–102, doi:10.1016/j.jhydrol.2009.12.020.
Chen, G.-Q., C. D. Levermore, and T.-P. Liu (1994), Hyperbolic conservation laws with stiff relaxation terms and entropy, *Commun. Pure Appl. Math.*, *47*(6), 787–830, doi:10.1002/cpa.3160470602.
Chertock, A., S. Cui, A. Kurganov, and T. Wu (2015), Well-balanced positivity preserving central-upwind scheme for the shallow water system with friction terms, *Int. J. Numer. Methods Fluids*, *78*, 355–383, doi:10.1002/fld.4023.
Costabile, P., C. Costanzo, and F. Macchione (2012), Comparative analysis of overland flow models using finite volume schemes, *J. Hydroinf.*, *14*(1), 122, doi:10.2166/hydro.2011.077.
Costabile, P., C. Costanzo, and F. MacChione (2013), A storm event watershed model for surface runoff based on 2D fully dynamic wave equations, *Hydrol. Processes*, *27*(4), 554–569, doi:10.1002/hyp.9237.
Delestre, O., S. Cordier, F. Darboux, and F. James (2012), A limitation of the hydrostatic reconstruction technique for Shallow Water equations, *C. R. Math.*, *350*(13–14), 677–681, doi:10.1016/j.crma.2012.08.004.
Di Giammarco, P., E. Todini, and P. Lamberti (1996), A conservative finite elements approach to overland flow: The control volume finite element formulation, *J. Hydrol.*, *175*(1–4), 267–291, doi:10.1016/S0022-1694(96)80014-X.
Duran, A. (2015), A robust and well-balanced scheme for the 2D Saint-Venant system on unstructured meshes with friction source term, *Int. J. Numer. Methods Fluids*, *78*, 89–121, doi:10.1002/fld.4011.
Duran, A., Q. Liang, and F. Marche (2013), On the well-balanced numerical discretization of shallow water equations on unstructured meshes, *J. Comput. Phys.*, *235*, 565–586, doi:10.1016/j.jcp.2012.10.033.
Fiedler, F. R., and J. A. Ramirez (2000), A numerical method for simulating discontinuous shallow flow over an infiltrating surface, *Int. J. Numer. Methods Fluids*, *32*(2), 219–240, doi:10.1002/(SICI)1097-0363(20000130)32:2⟨219::AID-FLD936⟩3.0.CO;2-J.
Fraccarollo, L., H. Capart, and Y. Zech (2003), A Godunov method for the computation of erosional shallow water transients, *Int. J. Numer. Methods Fluids*, *41*(9), 951–976, doi:10.1002/fld.475.
Garcia-Navarro, P., and M. E. Vazquez-Cendon (2000), On numerical treatment of the source terms in the shallow water equations, *Comput. Fluids*, *29*(8), 951–979, doi:10.1016/S0045-7930(99)00038-9.
George, D. L. (2008), Augmented Riemann solvers for the shallow water equations over variable topography with steady states and inundation, *J. Comput. Phys.*, *227*(6), 3089–3113, doi:10.1016/j.jcp.2007.10.027.
Govindaraju, R. (1988), On the diffusion wave model for overland flow: 1. Solution for steep slopes, *Water Resour. Res.*, *24*(5), 734–744.
Greenberg, J., and A. Leroux (1996), A well-balanced scheme for the numerical processing of source terms in hyperbolic equations, *SIAM J. Numer. Anal.*, *33*(1), 1–16, doi:10.1137/0733001.
Hou, J., Q. Liang, F. Simons, and R. Hinkelmann (2013a), A 2D well-balanced shallow flow model for unstructured grids with novel slope source term treatment, *Adv. Water Resour.*, *52*, 107–131, doi:10.1016/j.advwatres.2012.08.003.
Hou, J., Q. Liang, F. Simons, and R. Hinkelmann (2013b), A stable 2D unstructured shallow flow model for simulations of wetting and drying over rough terrains, *Comput. Fluids*, *82*, 132–147, doi:10.1016/j.compfluid.2013.04.015.
Hou, J., F. Simons, Q. Liang, and R. Hinkelmann (2014), An improved hydrostatic reconstruction method for shallow water model, *J. Hydraul. Res.*, *52*(3), 432–439, doi:10.1080/00221686.2013.858648.
Jin, S. (2012), Asymptotic preserving (AP) schemes for multiscale kinetic and hyperbolic equations: A review, *Rivista Mat. Univ. Parma*, *3*, 177–216.
Kesserwani, G., and Q. Liang (2011), A conservative high-order discontinuous Galerkin method for the shallow water equations with arbitrary topography, *Int. J. Numer. Methods Eng.*, *86*(1), 47–69, doi:10.1002/nme.3044.
LeFloch, P. G., and M. D. Thanh (2011), A Godunov-type method for the shallow water equations with discontinuous topography in the resonant regime, *J. Comput. Phys.*, *230*(20), 7631–7660, doi:10.1016/j.jcp.2011.06.017.
LeVeque, R. J. (1997), Wave propagation algorithms for multidimensional hyperbolic systems, *J. Comput. Phys.*, *131*(2), 327–353, doi:10.1006/jcph.1996.5603.
LeVeque, R. J. (1998), Balancing source terms and flux gradients in high-resolution Godunov methods: The quasi-steady wave-propagation algorithm, *J. Comput. Phys.*, *146*(1), 346–365, doi:10.1006/jcph.1998.6058.
Liang, D., R. A. Falconer, and B. Lin (2006), Improved numerical modelling of estuarine flows, *Proc. ICE: Mar. Eng.*, *159*, 25–35, doi:10.1680/maen.2006.159.1.25.
Liang, D., I. Özgen, R. Hinkelmann, Y. Xiao, and J. M. Chen (2015), Shallow water simulation of overland flows in idealised catchments, *Environ. Earth Sci.*, *74*(11), 7307–7318, doi:10.1007/s12665-015-4744-5.
Liang, Q. (2010), Flood simulation using a well-balanced shallow flow model, *J. Hydraul. Eng.*, *136*, 669–675.
Liang, Q., and A. G. L. Borthwick (2009), Adaptive quadtree simulation of shallow flows with wet-dry fronts over complex topography, *Comput. Fluids*, *38*(2), 221–234, doi:10.1016/j.compfluid.2008.02.008.
Liang, Q., and F. Marche (2009), Numerical resolution of well-balanced shallow water equations with complex source terms, *Adv. Water Resour.*, *32*(6), 873–884, doi:10.1016/j.advwatres.2009.02.010.
Liang, Q., J. Hou, and R. Amouzgar (2015), Simulation of Tsunami propagation using adaptive Cartesian grids, *Coastal Eng. J.*, *57*(04), 1550016, doi:10.1142/S0578563415500163.
Lighthill, M., and G. Whitham (1955), On kinematic waves. I. Flood movement in long rivers, *Proc. R. Soc. London Ser. A*, *229*(1178), 281–316.
Liu, T.-P. (1987), Hyperbolic conservation laws with relaxation, *Commun. Math. Phys.*, *108*(1), 153–175, doi:10.1007/BF01210707.
Mangeney, A., F. Bouchut, N. Thomas, J. P. Vilotte, and M. O. Bristeau (2007), Numerical modeling of self-channeling granular flows and of their levee-channel deposits, *J. Geophys. Res.*, *112*, F02017, doi:10.1029/2006JF000469.
Marche, F., P. Bonneton, P. Fabrie, and N. Seguin (2007), Evaluation of well-balanced bore-capturing schemes for 2D wetting and drying processes, *Int. J. Numer. Methods Fluids*, *53*(5), 867–894, doi:10.1002/fld.1311.
Morales De Luna, T., M. J. Castro Díaz, and C. Parés (2013), Reliability of first order numerical schemes for solving shallow water system over abrupt topography, *Appl. Math. Comput.*, *219*(17), 9012–9032, doi:10.1016/j.amc.2013.03.033.
Murillo, J., and P. García-Navarro (2010), Weak solutions for partial differential equations with source terms: Application to the shallow water equations, *J. Comput. Phys.*, *229*(11), 4327–4368, doi:10.1016/j.jcp.2010.02.016.
Murillo, J., P. Garcia-Navarro, J. Burguete, and P. Brufau (2007), The influence of source terms on stability, accuracy and conservation in two-dimensional shallow flow simulation using triangular finite volumes, *Int. J. Numer. Methods Fluids*, *54*, 543–590, doi:10.1002/fld.1417.
Rogers, B. D., A. G. L. Borthwick, and P. H. Taylor (2003), Mathematical balancing of flux gradient and source terms prior to using Roe's approximate Riemann solver, *J. Comput. Phys.*, *192*(2), 422–451, doi:10.1016/j.jcp.2003.07.020.

Rousseau, M., O. Cerdan, O. Delestre, and F. Dupros (2015), Overland flow modelling with the Shallow Water Equation using a well balanced numerical scheme: Better predictions or just more complexity?, *J. Hydrol. Eng.*, *20*(10), 04015012, doi:10.1061/(ASCE)HE.1943-5584.0001171.

Sanders, B. F., J. E. Schubert, and H. A. Gallegos (2008), Integral formulation of shallow-water equations with anisotropic porosity for urban flood modeling, *J. Hydrol.*, *362*(1–2), 19–38, doi:10.1016/j.jhydrol.2008.08.009.

Simons, F., T. Busse, J. Hou, I. Özgen, and R. Hinkelmann (2014), A model for overland flow and associated processes within the Hydroinformatics Modelling System, *J. Hydroinf.*, *16*, 375–391.

Singh, J., M. S. Altinakar, and Y. Ding (2015), Numerical modeling of rainfall-generated overland flow using nonlinear shallow-water equations, *J. Hydrol. Eng.*, *20*(8), 04014089, doi:10.1061/(ASCE)HE.1943-5584.0001124.

Song, L., J. Zhou, Q. Li, X. Yang, and Y. Zhang (2011a), An unstructured finite volume model for dam-break floods with wet/dry fronts over complex topography, *Int. J. Numer. Methods Fluids*, *67*, 960–980, doi:10.1002/fld.2397.

Song, L., J. Zhou, J. Guo, Q. Zou, and Y. Liu (2011b), A robust well-balanced finite volume model for shallow water flows with wetting and drying over irregular terrain, *Adv. Water Resour.*, *34*(7), 915–932, doi:10.1016/j.advwatres.2011.04.017.

Testa, G., D. Zuccalà, F. Alcrudo, J. Mulet, and S. Soares-Frazão (2007), Flash flood flow experiment in a simplified urban district, *J. Hydraul. Res.*, *45*, suppl. 1, 37–44, doi:10.1080/00221686.2007.9521831.

Teyssier, R. (2014), Grid-based hydrodynamics in astrophysical fluid flows, *Annu. Rev. Astron. Astrophys.*, *53*(1), 150619171245001, doi:10.1146/annurev-astro-082214-122309.

Toro, E. F. (2001), *Shock-Capturing Methods for Free-Surface Shallow Flow*, 309 pp., John Wiley, New York.

Wang, Y., Q. Liang, G. Kesserwani, and J. W. Hall (2011), A 2D shallow flow model for practical dam-break simulations, *J. Hydraul. Res.*, *49*(3), 307–316, doi:10.1080/00221686.2011.566248.

Yu, C., and J. Duan (2014), Two-dimensional hydrodynamic model for surface-flow routing, *140*(9), 1–13, doi:10.1061/(ASCE)HY.1943-7900.0000913.

Zhou, J. G., D. M. Causon, C. G. Mingham, and D. M. Ingram (2001), The surface gradient method for the treatment of source terms in the shallow-water equations, *J. Comput. Phys.*, *168*, 1–25, doi:10.1006/jcph.2000.6670.